RAMAN MEASUREMENTS OF TEMPERATURE DURING

CONTINUOUS WAVE LASER-INDUCED

HEATING OF SILICON

by

HO WAI LO

B.S., North Texas State University, 1976

A MASTER'S THESIS

Submitted in partial fulfillment of the

requirements for the degree

MASTER OF SCIENCE

Department of Physics

KANSAS STATE UNIVERSITY

Manhattan, Kansas

1979

Approved by:

Alvin Compaan

Major Professor

Spec. Coll.
LD
2668
.T4
1979
L64
c.2

TABLE OF CONTENTS

List of Figures . . . iii

List of Tables . . . iv

Acknowledgements. . . . v

INTRODUCTION . . . 1

THEORY . . . 4

Phonon Raman Scattering--Stokes and Anti-Stokes Intensity . . . 4

Temperature Dependence of the Raman Ratio in Silicon . . . 8

Temperature Rise Induced by a Laser Beam . . . 9

Maximum Linear Temperature Rise for a Gaussian Beam . . . 18

EXPERIMENTAL CONSIDERATIONS . . . 20

Laser . . . 20

Focusing and Collecting Optics, Power Measurements . . . 21

Sample and Sample Mounting . . . 27

Measurement of Beam Spot Size and Intensity Distribution . . . 27

Signal Detection and Data Acquisition. . . . 34

Beam Chopping . . . 37

RESULTS AND ANALYSIS . . . 41

Absorbed Power Density . . . 41

The Raman Data . . . 49

Corrections for Instrumental Efficiency. . . . 53

The ω^3 Correction . . . 54

Raman Ratio as a Function of Peak Temperature. . . . 54

Peak Temperature as a Function of Power Density . . . 59

SUMMARY AND CONCLUSIONS . . . 70

APPENDICIES

1. Program TCONV 72

2. Effect of Pinhole on the Observed Intensity in Beam Spot 73

3. Instrumental Efficiency Correction to the Raman Ratio: Polarized Radiation 79

4. Program TEMPRZ. 80

5. Program TEMPR 83

6. Program TTEMPR. 87

7. Program RATIO2. 89

8. Program RTCONV. 91

9. Program TPOWD 92

REFERENCES 93

ABSTRACT 97

LIST OF FIGURES

1. Recommended thermal conductivity in silicon 13
2. Calculated nonlinear temperature vs. linear temperature rise. 16
3. Focusing optics and collecting optics for Raman Signals 23
4. Collecting optics for specularly reflected radiation and power monitoring system 25
5. Two methods to measure beam spot size 30
6. Schematic diagram of the spectral throughput calibration of the Raman signal collection and detection system. 36
7. Raman signal detection system 39
8. Beam intensity profile for 514.5 nm beam. 43
9. Beam intensity profile for 457.9 nm component of all-line beam. 45
10. Beam intensity profile of all-line beam 47
11. First order Raman spectra at two different power densitites . . 51
12. Calculated temperature profiles and beam irradiance profiles in the radial and longitudinal directions 57
13. Calculated Raman ratio vs. peak temperature 61
14. Peak temperature vs. power density. 63
15. Geometry of pinhole in the beam spot. 75

LIST OF TABLES

1. Calculated Raman ratios as a function of peak temperature for W=30 and W=7.6 68

Acknowledgements

It is a pleasure to express my gratitude to my major professor, Alvin Compaan, for the invaluable guidance, help and inspiration he provided.

I am grateful to professor Tom Gray for serving on my committee and especially for his help and encouragement over the years.

I would like to thank also professor R.D. Dragsdorf for his help in the x-ray orientation of the samples and for serving on my committee. Many helpful discussions with professor Chris Sorensen are also gratefully appreciated.

To my wife Nessa, I offer very special thanks. Her patience, understanding and encouragement especially during the difficult times made this possible.

INTRODUCTION

Recently there has been considerable interest in the laser annealing of ion-implanted semiconductors.[1,2] In 1975, Soviet researchers Kachurin[3], Shytrkov[4] and co-workers reported the use of pulsed lasers for annealing of ion-implantation damaged semiconductors. Up until that time, thermal annealing in a furnace had been the only method available to repair the lattice disorder in materials caused by ion bombardments. Laser annealing offers many advantages over conventional thermal annealing. In addition to being a much faster process, laser annealing can be confined to the damaged (implanted) region to avoid the contamination and degradation associated with long term heating of the entire crystal. This feature is especially useful in the case of semiconductors such as GaAs that decompose at high temperatures. Most of the laser annealing work has been done on ion-implanted silicon[5], probably because of its widespread use in the fabrication of semiconductor devices. But some laser annealing has also been done on GaAs.[5] In both cases, there have been reports of excellent results in terms of restoration of crystal structure and electrical activity in the ion-implantation damaged semiconductor crystals.

As mentioned above, the earliest work in laser annealing was done using pulsed lasers. In 1976, Klimenko[6] and Kachurin[7] reported the use of scanning continuous wave (CW) Argon ion lasers for annealing. Today, both CW and pulsed techniques have been shown to be effective although some differences do exist in the annealed samples.[1] While pulsed laser annealing is a much faster process because of the very high power densities, secondary ion mass-spectrometry (SIMS) and ion backscattering experiments on the annealed samples revealed considerable redistribution of the implanted ions.[8,9] In contrast, no redistribution was observed in CW laser annealed samples.[10,11] This feature is important if the dopant profile is a critical requirement. Moreover, good focusing ability of the CW laser enables annealing in precise patterns such as in integrated circuits.

Although the technique of laser annealing shows great promise, researchers are still working towards an understanding of the physical processes involved. In the case of CW laser annealing, the absence of dopant redistribution plus reflectivity studies suggested a solid-phase epitaxial regrowth process in the amorphous (ion-implantation damaged) layers of silicon.[10] On the other hand, the basic mechanism of pulsed laser annealing is still the subject of much research.[12,13] For example, there has been much controversy on the question of whether melting of the sample surface is necessary for successful annealing by a pulsed laser.[14]

The temperature of the sample during laser heating is one important piece of information missing in the attempt to understand the kinetics and mechanism of the annealing process. Theoretical temperature calculations for the case of CW laser heating have been reported.[15,16] In fact these calculations have been utilized, in conjunction with epitaxial regrowth data obtained from conventional furnace anneal experiments, to prove that solid-state epitaxial regrowth is the basic mechanism in the CW laser annealing process. However, in addition to the fact that the calculated results have not been confirmed by experimental measurements, the accuracy of the calculations depends critically on a thorough knowledge of the properties of the material under different temperatures. There have also been reports of theoretical calculations of the sample temperature during pulsed laser heating[17] which involve numerical solutions of the heat transport equation. Again, no experimental temperature measurements are available to confirm the results.

In this thesis I shall demonstrate that it is possible to measure the sample temperature during laser heating by analyzing the Raman signals that are contained in the scattered radiation. In this method of temperature measurement, the heating beam can be used as the Raman excitation source. Alternatively, a small and low power probe beam (which would not cause significant heating) can be used to measure temperatures in different regions

of the sample. In principle, the temperature information is contained in the Raman signals through the temperature dependence of the phonon population. As will be explained later, the Raman anti-Stokes to Stokes intensity ratio is very simply related to the phonon population, making it easy to extract the temperature from the Raman ratio.

This thesis reports an experiment that demonstrates the feasibility of the Raman technique of temperature measurements. In the experiment, a focused CW argon ion laser is used to heat a pure silicon sample. The Raman ratios obtained are used to extract the maximum temperature as a function of absorbed laser power density. Because of limitations in the available laser power, the beam is focused very tightly to maximize power density and therefore the temperature. As a result, a Raman probe beam cannot be used. To account for the non-uniformity of temperature in the heated area, theoretical calculations of the thermal gradient are employed in the data reduction process.

For comparison purposes, calculated maximum temperatures based on Lax's solution to the heat conduction equation[15,16] are also presented. The results show good agreement between theory and experimental data. Finally, possible reasons for the small difference that do exist between theory and experiment are discussed. Because of the good results obtained in this investigation, the Raman method appears to be a very promising technique for temperature measurements during laser heating.

THEORY

Phonon Raman Scattering--Stokes and Anti-Stokes Intensity

Raman scattering is the inelastic scattering of photons. In first order phonon Raman scattering in crystals, an incident photon of energy $\hbar\omega_i$ is destroyed resulting in the creation of a scattered photon of energy $\hbar\omega_s$, accompanied by the creation or destruction of a phonon of energy $\hbar\Omega$. Requirements of energy and wave vector conservation in the process give rise to the following selection rules:

$$\omega_i = \omega_s \pm \Omega \tag{1}$$

$$\vec{k}_i = \vec{k}_s \pm \vec{q} \tag{2}$$

where $\vec{q}$ is the phonon wave vector. The positive sign applies to the case of phonon creation (Stokes process) while the negative sign refers to the destruction of an existing phonon (anti-Stokes process). The fact that phonon frequencies are usually much smaller than photon frequencies ω_i or ω_s leads to the approximations $\vec{k}_i \approx \vec{k}_s$ and $|\vec{q}| \approx 2|\vec{k}_i|\sin(\frac{\phi}{2})$ where ϕ is the angle between the incident and scattered photons. For a typical incident photon of wavevector of the order of 10^5 cm^{-1} in a crystal, conservation of wavevector restricts the wavevector of the scattered phonon to be also of the same order of magnitude. Compared with the typical Brillouin Zone widths of 10^8 cm^{-1}, the Raman phonons are essentially zone-center phonons.

The intensity of the Raman lines in crystals can be found most directly using the third order time dependent perturbation theory. The procedure, which was first employed by Loudon[18] in calculations for diamond and zincblend structure crystals, considers the elementary interactions between three systems: the photons, the electrons and the lattice. For the case of Stokes scattering in which a phonon is created, the probability per unit time that an incident photon is destroyed in a Raman process is given by[18]

$$\frac{1}{\tau} = \frac{2\pi}{\hbar^6} \sum_{\vec{q},\vec{k}_s} \left| \sum_{\alpha,\beta} \frac{\langle n_i-1,\ 1;\ n_0+1;\ 0|H_I|\beta\rangle\langle\beta|H_I|\alpha\rangle\langle\alpha|H_I|n_i,0;\ n_0;\ 0\rangle}{(\omega_\alpha-\omega_i)(\omega_\beta-\omega_i)} \right|^2 \times \delta(\omega_i-\Omega-\omega_s) \tag{3}$$

where n_i, 0, n_o are the populations of incident photons, scattered photons and optic phonons in the initial state; α and β are the intermediate states of the system; $\vec{q}$, $\vec{k}_s$ are the phonon and scattered photon wavevectors. Moreover, the electronic system starts and ends in the ground state. The interaction matrix consists of two parts: $H_I = H_{ER} + H_{EL}$, where H_{ER}, the electron-photon interaction, contributes to the first and third matrix elements, while H_{EL}, the electron-lattice interaction, contributes to the second matrix element. Here H_{RL}, the photon-lattice interaction, has been neglected assuming a very large difference between photon and phonon energies and therefore weak interactions (in our case, the zone center phonon energy of silicon is 64 meV compared with the typical laser photon energy of 2.5 eV). H_{ER} is given, in second quantized symbols,[18]

$$H_{ER} = \frac{e}{m} \sum_j \sum_k \left(\frac{2\pi\hbar}{\eta V \omega_k}\right)^{1/2} \left[a_k^- e^{i\vec{k}\cdot\vec{r}_j} + a_k^+ e^{-i\vec{k}\cdot\vec{r}_j}\right] \vec{\varepsilon}_k \cdot \vec{p}_j \quad (4)$$

where $\vec{p}_j$, $\vec{r}_j$ are the momentum and position vectors for the jth electron, η is the optical dielectric constant, V is the crystal volume, $\hat{\varepsilon}_k$ is the unit polarization vector of the photon $\vec{k}$, a_k^- and a_k^+ are the destruction and creation operators for the photon of energy $\hbar\omega_k$. The matrix elements of H_{EL} for non-polar crystals such as silicon can be expressed in terms of the deformation potential $\Xi^i_{\alpha\beta}$ as:[18]

$$\langle\beta|H_{EL}|\alpha\rangle = \Xi^i_{\alpha\beta} \left(\frac{\hbar}{2\mu N \omega_{s\vec{q}} a^2}\right)^{1/2} \hat{\xi}_{s\vec{q}}\, e^{i\vec{q}\cdot\vec{R}} \left(b^+_{s-\vec{q}} + b^-_{s\vec{q}}\right) \quad (5)$$

where μ is the reduced mass of the atoms in the unit cell, N is the number of unit cells in the crystal, $\hat{\xi}_{s\vec{q}}$ is the unit directional vector dependent on the optic phonon $s\vec{q}$, $\vec{R}$ is the position vector of the sublattices, b^+ and b^- are the creation and destruction operators for the phonon, and a is the lattice constant. Evaluation of the matrix elements yields the following expression for the Stokes scattering probability[18]

$$\frac{1}{\tau} = \frac{4\pi^3 e^4}{\hbar^3 m^4 \eta^2 a^2 \mu N} \sum_{\vec{q},\vec{k}_s} \frac{n_i(n_o+1)}{\Omega\omega_i\omega_s} \left|\hat{\xi}^i_{o\vec{q}} R^i_{12}(-\omega_i,\omega_s,\Omega)\right|^2 \times \frac{(2\pi)^3}{V} \delta(\vec{k}_i - \vec{q} - \vec{k}_s)\,\delta(\omega_i - \Omega - \omega_s) \quad (6)$$

with the Raman tensor

$$R^{i}_{12}\ (-\omega_i,\omega_s,\Omega) = \frac{1}{V}\sum_{\alpha,\beta}\left[\frac{p^{2}_{o\beta}\ \Xi^{i}_{\beta\alpha}\ p^{1}_{\alpha o}}{(\omega_\beta+\Omega-\omega_i)(\omega_\alpha-\omega_i)} + \text{five terms}\right] \tag{7}$$

where $p_{o\beta}=\langle o|\vec{p}|\beta\rangle$, $p_{\alpha o}=\langle\alpha|\vec{p}|o\rangle$ are the momentum matrices. The superscripts 1,2 denote the polarization directions $\hat{\varepsilon}_1,\hat{\varepsilon}_2$ of the photons ω_i,ω_s. In the above expression, (n_o+1) is the phonon population factor produced as a result of the phonon creation operator. The six terms in the Raman tensor correspond to the six possible time orderings in the interactions between the three systems. However, for homopolar crystals (such as silicon) which does not have infrared-active (long wavelength) phonons, only the first term which corresponds to the process described in the following diagram is of significance because the energy denominator in the first term is much smaller than that of the other terms.[19]

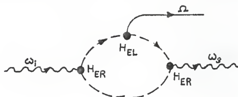

The anti-Stokes scattering probability is given by an expression very similar to the Stokes probability

$$\frac{1}{\tau} = \frac{4\pi^3 e^4}{\hbar^3 m^4 n^2 a^2 \mu N}\sum_{\vec{q},\vec{k}_s}\frac{n_i n_o}{\Omega\omega_i\omega_{as}}\left|\hat{\xi}^{i}_{o\vec{q}}\ R^{i}_{12}\ (-\omega_i,\omega_{as},-\Omega)\right|^2 x\frac{(2\pi)^3}{V}\ \delta(\vec{k}_i+\vec{q}-\vec{k}_{as})\,\delta(\omega_i+\Omega-\omega_{as}) \tag{8}$$

and $$R^{i}_{12}\ (-\omega_i,-\omega_{as},\Omega) = \frac{1}{V}\sum_{\alpha,\beta}\frac{p^{2}_{o\beta}\ \Xi^{i}_{\beta\alpha}\ p^{1}_{\alpha o}}{(\omega_\beta-\Omega-\omega_i)(\omega_\alpha-\omega_i)} \tag{9}$$

where the subscript as denotes the anti-Stokes quantities. In addition to the differences in the scattered photon frequency ω_s and the phonon occupation number n_o, the Stokes and anti-Stokes probabilities differ in the Raman tensors. However, the difference between the Raman tensors, which lies mainly in the energy denominators$(\omega_\beta\pm\Omega-\omega_i)$, is small provided that the incident photon

frequency ω_i is not close to any transition frequency ω_β. Concentrating only on the quantities that are different between the Stokes and anti-Stokes cases, and carrying out the summations, the scattering probabilities can be written as follows:

$$\left(\frac{1}{\tau}\right)_{\text{Stokes}} \propto (n_o+1)(\omega_i-\Omega)\left|R^i_{12}\ (-\omega_i,\omega_s,\Omega)\right|^2 \tag{10}$$

$$\left(\frac{1}{\tau}\right)_{\text{A-Stokes}} \propto (n_o)(\omega_i+\Omega)\left|\ R^i_{12}\ (-\omega_i,\omega_{as},-\Omega)\right|^2 \tag{11}$$

As mentioned above, the differences between the Raman tensors are small, but they are kept in the above expression because of the ω_s dependence contained in the $p_{0\beta}$ matrix. For dipole transitions, the frequency dependence of the matrix can be extracted by changing to the length formulation:[20]

$$<0|\vec{p}|\beta> = -im\omega_s<0|\vec{D}|\beta> \tag{12}$$

where $\vec{D}$ is the electronic displacement vector. Consequently, the ratio of the number of Stokes scattered photons N_S to the number of anti-Stokes photons N_A per unit time is

$$\frac{N_S}{N_A} = \left(\frac{n_o+1}{n_o}\right)\left(\frac{\omega_i-\Omega}{\omega_i+\Omega}\right)^3 \tag{13}$$

where $n_o=n_o(\Omega)$ is the initial phonon population described by photon statistics:

$$n_o=\left(e^{\hbar\Omega/kT} - 1\right)^{-1} \tag{14}$$

It should be pointed out that the above ratio is of the number of photons. If the ratio of intensities is needed, the expression must be multiplied by a ratio of the photon energies $\left(\frac{\omega_i-\Omega}{\omega_i+\Omega}\right)$, giving rise to the usual ω^4 dependence of dipole radiation. However, when the Raman radiation is detected by a photomultiplier, the number, not energy, of photons are counted, and the ω^3 expresssion is applicable.

It should also be mentioned that equation (13) was derived assuming negligible difference between the Raman tensors after the ω_s dependence in $p_{0\beta}$ was

extracted. The remaining difference, which lies mainly in the energy denominator $(\omega_\beta \pm \Omega - \omega_i)$, is negligible provided $\Omega << |\omega_\beta - \omega_o|$. According to Renucci et al,[21] the condition $\Omega << |\omega_\beta - \omega_o|$ is indeed valid down to near resonance conditions for the zone center phonon in silicon. Therefore the above expression for the Raman ratio is applicable for our case.

Temperature Dependence of the Raman Ratio in Silicon

Many expreiments have been performed concerning the lattice dynamics in silicon.[22] With the diamond crystal structure, silicon has only one first-order Raman-active optical phonon located at the Brillouin zone center. In group theoretical symbols, this optical phonon belongs to the irreducible representation Γ_{25}'. Moreover, being a homopolar crystal, the longitudinal and transverse optical phonons are degenerate at the zone center. The energy of this optical phonon was determined experimentally both by neutron scattering data and from one-phonon Raman studies, with the most accurate value to date being 519 cm^{-1} at room temperature obtained by the Raman studies.[22]

Temperature dependence of the Raman spectra in silicon was first investigated experimentally by Hart et al.[23] In the experiment, the temperature dependence of the linewidth, frequency and Raman intensity ratio of the zone center optical phonon were studied over the temperature range of 20 - 770^oK. In the experiment, silicon samples with a mirror-like (111) face were uniformly heated to eight different temperatures over the temperature range mentioned above. Moreover, a relatively low power density of ≈ 200 W/cm^2 from the 514.5 nm line of an argon ion CW laser was used throughout the experiment to avoid laser heating effects. The temperature dependence of the Raman intensity ratio was compared with that predicted by Bose-Einstein statistics:

$$R = \frac{I_{Anti-Stokes}}{I_{Stokes}} = \frac{n_o}{n_o+1} = e^{-\hbar\Omega/kT} \quad (15)$$

The result was that the experimental points fall consistently above the theoretical curve. This discrepancy between experimental data and the theory was later

resolved by Anastassakis et al.[24] who pointed out that the ω^4 correction must be made to the experimental data before comparison with theory. As mentioned in the last section, the intensity of the Raman radiation is proportional to the fourth power of the frequency. In the case of large phonon frequencies, this ω^4 correction to the intensity ratio can be significant. For the 519 cm^{-1} optical phonon and for a typical laser excitation frequency of 20,000 cm^{-1} (500 nm wavelength), the ω^4 correction factor is $\simeq 0.8$. Applying this correction to the intensity ratio obtained by Hart, it can be shown that the data points are in good agreement with theory. Consequently, the Raman intensity ratio is indeed a valid probe of temperature in silicon.

Temperature Rise Induced by a Laser Beam

Theoretical calculations of the temperature rise in a solid sample during CW laser irradiation (steady-state conditions) have been done by Lax.[15,16] The calculations are useful in this study for two reasons. In addition to being a guideline to the experimental results, the calculations provided information which is necessary for data reduction because of the following situation. The finite size of the beam spot on the sample, combined with a non-uniform beam intensity profile, inevitably produce temperature gradients on the sample. Moreover, the low thermal conductivity values of silicon create large thermal gradients which cannot be neglected even within the extremely small beam spots ($\approx$ 10 microns) applied in our experiment. Consequently, the Raman signal collected during the experiment is a collection of signals originating from different temperature regions on the sample. In order to extract the maximum temperature rise from the experimental data, therefore, it is necessary to know the temperature gradient wherever light scattering occurs. In principle, such information can be obtained experimentally by collecting signals from selected regions of the same temperature or by using a small probe beam of very low intensity. However, the very small size of the beam spot and the relatively

low power of the argon laser used in this experiment make it very difficult in practice. The theoretical thermal gradients, although not experimentally verified, provide the best estimate under these circumstances. Moreover, for a beam intensity profile which is heavily weighted towards the center (such as the Gaussian beam profile), small errors in the thermal gradient should not greatly affect the final results.

Although Lax's[15,16] theoretical accounts of the problem of laser induced heating has been published, it is useful to reproduce the steps leading to the results and, especially importantly, to point out the assumptions that entered the calculations. In fact, a critical study of the calculations should be most helpful during the process of data analysis.

Physically, the problem involves a radially symmetric beam spot on the sample which is very large compared with the beam area. It is also assumed in the calculations that the attenuation length (inverse of the absorption constant) for the incident radiation is much smaller than the thickness of the sample. The medium can therefore be treated as semi-infinite. The dominant heat dissipation mechanism in the steady-state process is assumed to be thermal conduction alone. This is possible provided the high temperature region on the sample is so small that heat loss due to radiation and convection is negligible compared with heat conduction through the back of the sample. Moreover, it is assumed that the absorption constant does not change with temperature variations. In semiconductors such as silicon, the absorption constant is quite sensitive to large temperature changes even for photon energies well above the direct energy band gap. It is therefore doubtful that this assumption of a temperature invariant absorption constant is valid for our case. However, it can be shown from the calculations that for the special cases of spot sizes large compared with the attenuation length, the temperature rise is quite insensitive to variations of the absorption constant.

In the first of the two papers by Lax, calculations were performed assuming

constant thermal conductivity. However, this restriction was relaxed as the second paper took into account temperature variations of the thermal conductivity. In fact, provided that the thermal conductivity values are known as a function of temperature (nonlinear case), it was shown that the problem could be very simply related to the case of constant thermal conductivity (linear case). This feature is of great importance in laser heating of silicon because the thermal conductivity near the melting point is reduced by a factor of 8 from the room temperature value. Figure 1 shows the recommended values of thermal conductivity in silicon in the temperature range from $300^{o}K$ to $1685^{o}K$ (melting point).[25]

The starting point of the calculations is the continuity equation with a source:

$$\frac{\partial\rho}{\partial t} + \mathrm{div.}\ \vec{J} = G \tag{16}$$

where G is the heat input per unit volume per unit time, ρ is the heat density and $\vec{J}$ is the heat flux. With conduction as the only heat dissipation mechanism, the flux is given by[26]

$$\vec{J} = -K\vec{\nabla}T \tag{17}$$

where K is the thermal conductivity and T is the temperature. The heat density ρ can be expressed in terms of the heat capacity per unit volume C as $\rho = CT$, then the continuity equation becomes the conduction equation:

$$C\frac{\partial T}{\partial t} - \mathrm{div}[K(T)\vec{\nabla}T] = G(\vec{r}) \tag{18}$$

If K is independent of temperature (linear case), the conduction equation is

$$C\frac{\partial T}{\partial t} = K\nabla^{2}T + G \tag{19}$$

The nonlinear conduction equation can be reduced to the linear type by introducing a "linear" temperature Θ:

$$\Theta(T) \equiv \int_{T_0}^{T} \frac{K(T)}{K_0}\, dT \tag{20}$$

where $K_0 \equiv K(T_0)$ and T_0 is the room temperature as will be shown in the following development. Using the previously mentioned recommended thermal conductivity values,

FIGURE 1

Recommended thermal conductivity in silicon in the temperature range of 300 to 1685°K.

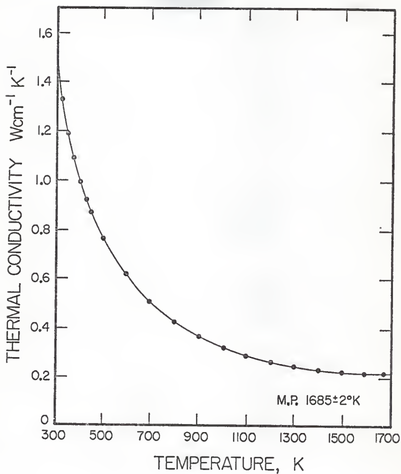
THERMAL CONDUCTIVITY Wcm^{-1} K^{-1}
1.6
1.4
1.2
1.0
0.8
0.6
0.4
0.2
0
300
500
700
900
1100
1300
1500
1700
TEMPERATURE, K
M.P. 1685±2°K

a computer program TCONV (see appendix 1) was written following equation (20) to generate a curve relating the linear temperature rise to the nonlinear (real) temperatures. Figure 2 shows the resulting curve. With the above transformation, the linear conduction equation is obtained:

$$C\frac{\partial \Theta}{\partial t} = \text{div.} (K_0 \vec{\nabla} \Theta) + G \qquad (21)$$

Since there is a one-to-one correspondence between the linear and nonlinear (real) temperatures, solutions to the linear equation can be converted to the nonlinear case through the knowledge of K(T).

Under steady-state conditions, the time-dependent term in the equation can be removed to yield:

$$\nabla^2 \Theta = \frac{-G(r,z)}{K_0} \qquad (22)$$

The heat source G has cylindrical symmetry for a radially symmetric beam spot and a uniform, homogeneous medium:

$$G(r,z) = \alpha I_0 e^{-\alpha z} f(r) \qquad (23)$$

where α is the absorption constant, I_0 is the maximum irradiance of the laser beam (absorbed), z is distance into the sample, and f(r) is the radial intensity distribution function for the beam spot. For a Gaussian beam, $f(r)=\exp(-r^2/a^2)$ where a is the 1/e radius of the beam waist.

To further generalize the equation, the variables can be made unitless by choosing a as a unit of length,

$$R \equiv {}^{r}/a \qquad Z = {}^{z}/a \qquad W = \alpha a \qquad (24)$$

Then the equation becomes

$$\nabla^2 \Theta(R, Z) = \frac{-G(R,Z)}{K_0} = \frac{-\alpha I_0 a^2 e^{-WZ}}{K_0} f(R) \qquad (25)$$

Looking for homogeneous solutions, the equation can be separated into R and Z parts with separation constant λ^2. The equation involving Z can be solved immediately yielding an exponentially decaying function while the R equation is just the Bessel equation in the zeroth order. Since the temperature must

FIGURE 2

Calculated nonlinear temperature as a function of linear temperature rise from room temperature.

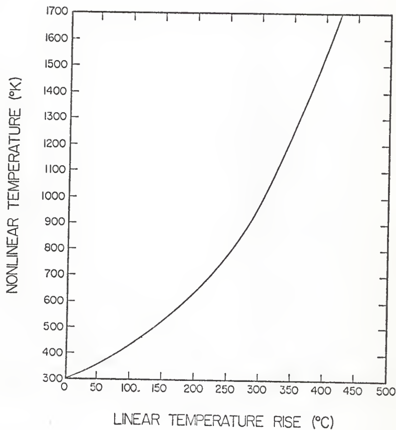
1700
1600
1500
1400
1300
1200
1100
1000
900
800
700
600
500
400
300
NONLINEAR TEMPERATURE (°K)
0
50
100.
150
200
250
300
350
400
450
500
LINEAR TEMPERATURE RISE (°C)

remain finite at R=0, the only solutions to the radial equation are the zeroth order Bessel functions. The homogeneous solution is therefore

$$\Theta_{homo} = \int_0^\infty e^{-\lambda Z} J_0(\lambda R) g(\lambda) \lambda d\lambda \quad (26)$$

where $g(\lambda)$ is a function determined by boundary conditions at the sample surface (Z=0). Moreover, λ is continuous and unrestricted (excepted that it be real and positive) because the sample is assumed to be semi-infinite.

To obtain a particular solution, the method of eigenfunction expansion was employed. The differential operator in the R equation has normalized and continuous eigenfunctions $J_0(\lambda R)$:

$$\left[\frac{1}{R}\frac{d}{dR}\left(R\frac{dv}{dR}\right) + W^2\right] J_0(\lambda R) = (W^2-\lambda^2) J_0(\lambda R) \quad (27)$$

By inspection, the particular solution can be written in the following form:

$$\Theta_{part} = e^{-WZ} v(R) \quad (28)$$

Substitution of this solution back into the differential equation yields an equation for v(R):

$$\frac{1}{R}\frac{d}{dR}\left(R\frac{dv}{dR}\right) + W^2 v = -Bf(R) \ ; \ B \equiv \frac{\alpha I_0 a^2}{K_0} \quad (29)$$

The functions f(R) and v(R) can be expanded in terms of the eigenfunctions:

$$f(R) = \int_0^\infty J_0(\lambda R)\ F(\lambda) \lambda d\lambda \quad (30)$$

and

$$v(R) = \int_0^\infty J_0(\lambda R)\ V(\lambda) \lambda d\lambda \quad (31)$$

where $F(\lambda)$, $V(\lambda)$ are the Hankel transform functions[27] of f(R) and v(R) respectively. For a given heat source distribution, $F(\lambda)$ is known

$$F(\lambda) = \int_0^\infty J_0(\lambda R)\ f(R) R dR \quad (32)$$

$V(\lambda)$ can then be found by substitution back into the differential equation. The particular solution is therefore

$$\Theta_{part} = -Be^{-WZ} \int_0^\infty \frac{J_0(\lambda R) F(\lambda) \lambda d\lambda}{W^2-\lambda^2} \quad (33)$$

The unknown function $g(\lambda)$ can now be found by imposing the boundary condition at the sample surface. For negligible heat loss to air from the surface,

$$\frac{\partial\Theta}{\partial Z}\Big|_{Z=0} = \left[\frac{\partial\Theta_{homo}}{\partial Z} + \frac{\partial\Theta_{part}}{\partial Z}\right]_{Z=0} = 0 \tag{34}$$

Finally, the solution to the linear equation is:

$$\Theta(R,Z,W)=B\int_0^\infty J_0(\lambda R)F(\lambda)\frac{We^{-\lambda Z}-\lambda e^{-WZ}}{W^2-\lambda^2}\,d\lambda \tag{35}$$

The differential equation and the boundary conditions are satisfied if a constant term is added to the above expression. Recalling the relationship between T and Θ ,

$$\int_{T_0}^{T}\frac{K(T)}{K_0}\,dT = B\int_0^\infty J_0(\lambda R)F(\lambda)\frac{We^{-\lambda Z}-\lambda e^{-WZ}}{W^2-\lambda^2}\,d\lambda + \text{constant} \tag{36}$$

It is most convenient to adjust T_0 such that the constant is zero. If no heat source is present, B=0 and T= room temperature. Therefore T_0 is the room temperature. Moreover, in choosing the constant to be zero, $\Theta(R,Z,W)$ is the "linear" temperature rise cause by the heating beam.

It would be convenient to express the temperature in terms of the absorbed power P:

$$P = I_0\int_0^\infty f(R)2\pi r dr = 2\pi I_0 a^2\int_0^\infty f(R)RdR = 2\pi I_0 a^2 F(0) \tag{37}$$

then

$$\Theta(R,Z,W) = \frac{\alpha P}{2\pi K_0 F(0)}\int_0^\infty J_0(\lambda R)F(\lambda)\frac{We^{-\lambda Z}-\lambda e^{-WZ}}{W^2-\lambda^2}\,d\lambda \tag{38}$$

The Maximum Linear Temperature Rise for a Gaussian Beam

For a Gaussian beam intensity distribution, the maximum temperature rise occurs on the surface and at the beam center (R=Z=0),

$$\Theta(0,0,W) = \frac{\alpha P}{2\pi K_0 F(0)}\int_0^\infty \frac{F(\lambda)d\lambda}{W+\lambda} \tag{39}$$

For a Gaussian function, the Hankel transform $F(\lambda)=\frac{1}{2}e^{-\frac{1}{4}\lambda^2}$, therefore

$$\Theta(0,0,W)= \frac{\alpha P}{2\pi K_0}\int_0^\infty \frac{e^{-\frac{1}{4}\lambda^2}}{W+\lambda}\,d\lambda \tag{40}$$

Although it appears natural to normalize the temperatures to the maximum value, Lax considered it more convenient and revealing to normalize the temperature to the absolute maximum temperature value when W approaches infinity, which corresponds to the case of very large absorption constant (as in a metal) or very large beam spot size compared with the absorption length:

$$\Theta_{max}(0,0,\infty)= \frac{\alpha P}{2\pi K_o W} \int_o^\infty e^{-\frac{1}{4}\lambda^2}\, d\lambda = \frac{P}{2\sqrt{\pi} K_o a} \tag{41}$$

Defining N(R,Z,W) such that $\Theta(R,Z,W) = \Theta_{max} N(R,Z,W)$,

$$N(R,Z,W)= \frac{W}{\sqrt{\pi}} \int_o^\infty J_o(\lambda R) e^{-\frac{1}{4}\lambda^2} \frac{We^{-\lambda Z}-\lambda e^{-WZ}}{W^2-\lambda^2}\, d\lambda \xrightarrow[W\to\infty]{R,Z=0} 1 \tag{42}$$

Lax in his paper included results of numerical calculations of N(R,Z,W) for several values of W. It was shown that when W=26, the value of N(0,0,26) is approximately 0.95 which is quite close to the limiting value ($W\to\infty$) of 1. For a typical radiation wavelength of 500 nm, the absorption length of silicon at room temperature is about 1 micron.[28] Therefore a rather small beam spot of radius, say 50 microns, can bring the linear temperature profile to approach the limiting case of $W\to\infty$.

EXPERIMENTAL CONSIDERATIONS

Laser

This experiment was performed using a Coherent Radiation Model 52 argon ion CW laser which provided both the heating beam and the excitation radiation for the Raman studies. Both single-line and all-line operations were used depending on the power level required. For low power data points, the laser was tuned to the 514.5 nm line with an intracavity prism wavelength selector. Power variations were achieved by adjusting the laser current. However, the maximum power output of about 1.4 Watts with this single line operation could not produce sample-melting power densities with the focusing optics used. Therefore all-line operation, which could deliver a maximum output power of about 3.5 Watts, was used for higher power data points. The power distribution of the lines in the all-line laser spectrum was experimentally measured through separating the lines by a prism (outside the laser) and then measuring the power of each line with a photovoltaic cell. The following table shows the relative intensities of the lines as a result of the measurements:

Wavelength (nm)	Relative Intensity
457.9	0.065
476.5	0.29
488.0	0.94
496.5	0.25
501.7	0.15
514.5	1.00

Operating in the multi-line mode, the laser spectrum had a weighted average of 496.5 nm which was reasonably close to the single-line 514.5 nm in terms of heating effects. Again different power levels were obtained by varying the laser current. Moreover, sample-melting was achieved before the laser reached maximum power. With all-line operation, the 514.5 nm line could no longer be used as excitation radiation for Raman scattering studies due to

the following reason. Because of the relatively large phonon energy of about 520 cm^{-1}, the Raman signals occur in the proximity of the laser lines neighboring the 514.5 nm line, giving rise to laser fluorescence problems. This undesirable situation also applied to other relatively high-powered laser lines such as the 488 nm line. Scanning through all the available lines, it was found that only the 457.9 nm line could be used for Raman scattering purposes. Due to this relatively weak laser excitation (the power of the 457.9 nm line is only 2.4% of the total all-lines output), the intensity of the Raman signal suffered. However, uncertainties arising from weak Raman signals were brought down to acceptable levels by longer counting times and by integration over the Raman peaks.

Room temperature data of Dash and Newman[28] show that the absorption constant of silicon at 457.9 nm (2.08×10^4 cm^{-1}) is larger than that at 514.5 nm (1.0×10^4 cm^{-1}). However, this large difference in the absorption lengths for the two Raman excitation radiation used in the experiment did not cause problems. As will be discussed in the section on data analysis, the absorption lengths at these experimental laser frequencies are small enough that the laser intensity decays much faster than the temperature in the longitudinal direction (into the sample). In other words, all the Raman signals detected essentially originated from the surface of the sample.

Focusing and Collecting Optics, Power Measurements

Figure 3 shows the schematic diagram of the focusing optics and the collecting optics for the Raman signals. The focusing lens was a coated, achromatic spherical lens of 5 cm focal length. With a diameter of about 1.5 cm, the lens was reasonably large compared with the 0.3 cm laser beam width so that lens aberration was not serious. At the focus of the lens, the beam waist was about 10 microns in diameter. The sample was mounted such that the surface was at or very near the beam focus. Moreover, near normal incidence (5° to normal) was used to ensure a uniform beam spot.

FIGURE 3

Focusing optics and collecting optics for the Raman signals.

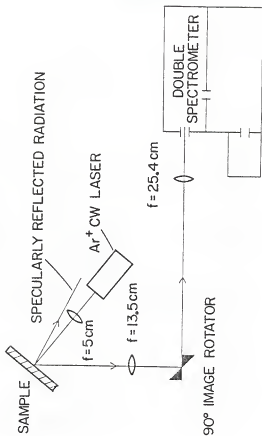
SAMPLE
SPECULARLY REFLECTED RADIATION
Ar$^+$ CW LASER
f = 5 cm
f = 13.5 cm
f = 25.4 cm
DOUBLE SPECTROMETER
90° IMAGE ROTATOR

FIGURE 4

Collecting optics for specularly reflected radiation and power monitoring system. Dashed lines show position of beam splitter when laser power (incident and reflected) were measured.

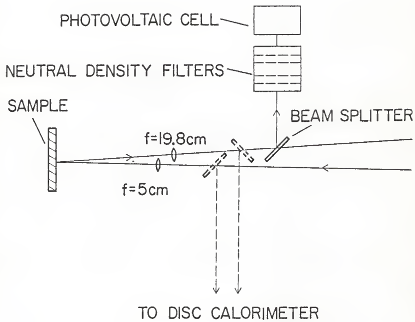
PHOTOVOLTAIC CELL
NEUTRAL DENSITY FILTERS
SAMPLE
BEAM SPLITTER
f=19.8cm
f=5cm
TO DISC CALORIMETER

Scattered Raman signals were collected at 60^{0} relative to the incident beam, well away from the strong, specularly reflected radiation. The collection lens was a multielement Vemar Telephoto lens (f=135 mm) with the aperture set at f/2.8 when Raman data were taken. Coupled with the 25.4 cm focusing lens in front of the spectrometer slits, the collection optics produced at the entrance slits of the spectrometer an image magnification of ≈ 2 for the beam spot on the sample.

In order to determine the power absorbed by the sample, the power of both the incident laser radiation and the specularly reflected radiation were measured. Figure 4 shows the experimental set-up for the collecting and power-monitoring optics for the specularly reflected radiation. Power measurements were done at the beginning and conclusion of each set of data with a Scientech Model 3600 Disc Calorimeter which had a uniform spectral response from 0.3 to 30 microns and a useful power range from 1 mW to 3 Watts. To avoid damaging the disc calorimeter and for convenient positioning of the power meter, a beam splitter was put in the beam and the power of the reflected portion (at 90^{0} with respect to the beam) was measured. At the operating laser frequencies, the power of the reflected portion from the beam splitter was measured to be 15.5% that of the incident beam. Moreover, the transmittance of two lenses in the path of the incident and reflected beams were measured and found to be the same at 95% for the operating laser frequencies.

In addition to the power measurements before and after each run, the power of the reflected beam was continuously monitored for stability by using a photovoltaic cell. The beam splitter in front of the photovoltaic cell was used to position the beam onto the cell and to attenuate the beam. Moreover, neutral density filters were used when necessary to avoid saturation or damage to the cell. The output of the cell was fed through an amplifier circuit and displayed on a milliammeter. Under steady-state conditions,

the stability of the reflected power should be indicative of the stability of the incident laser power. During the experiments, it was observed that with adequate warm-up of the laser, power fluctuations were generally below 2%.

Sample and Sample-Mounting

The sample used was a pure, unimplanted silicon wafer roughly 5 cm in diameter and 0.4 mm thick. Sample resistivity was approximately 5000 Ω-cm. The sample surface was mechanically polished to a mirror-like finish. Before the experiment and from time to time thereafter, the sample was carefully cleaned with acetone to remove any dirt and oil film accumulated as a result of exposure to air. The sample was attached to a chuck with a very thin layer of Duco cement and then mounted on translation stages which provided transverse and vertical movements in the plane of the sample surface. With this translational freedom, the sample could be moved without disturbing the focusing configurations. This feature was necessary to allow the laser beam to avoid any damage spots or imperfections on the surface caused by previous laser melting or residual scratches from the polishing procedure. The sample was exposed to air throughout the experiment under room temperature of about 300°K to simulate laser annealing conditions.

Crystal orientation performed using X-ray Laue techniques showed that the sample had a (111) face. The sample was mounted such that the incident laser radiation (vertically polarized) was polarized along the $[\bar{1}01]$ direction.

Measurement of Beam Spot Size and Intensity Distribution

With the power density being an independent variable in the experiment, accurate measurement of the beam spot size on the sample is necessary. In this experiment, two methods were employed to ensure proper accuracy. A common method which can measure the spatial distribution of laser power in the spot is to map the power coming through a scanning pinhole which is confined to move in the focal plane of the focusing lens. However, this method was not

employed for two reasons: the size of the spot (≈ 10 μm) was too small to be scanned by a pinhole, and it would be very difficult to position the pinhole at the exact position where the sample was placed. Instead, a modified version of the method was used. Since the two factors that affect the spot size, diffraction and beam divergence, both scale directly with the focal length of the focusing lens, the spot size produced by a long focal length lens (f=57.1 cm) was first found using the above mentioned method. Then the actual spot size on the sample was obtained by multiplying this 'large' spot size by the ratio 5/57.1 since the actual focusing lens had a focal length of 5 cm. Figure 5a shows the schematic for the above mentioned measurement procedure. Two translation stages mounted at right angles provided two dimensional freedom of movement for the pinhole (diameter=25 microns). Detection of the radiation coming through the pinhole was by a photovoltaic cell connected to a millivoltmeter. In operation, the pinhole was first positioned at the center of the beam spot indicated by a maximum signal on the voltmeter. Then using the graduated micrometer on the translation stage, the pinhole was scanned horizontally from one end of the spot to the other at 25 micron intervals, with the voltmeter reading recorded at each step. To ensure that the pinhole was in the focal plane of the lens, the lens was moved to different positions in the line of the laser beam and the above procedure repeated until the smallest spot size was observed. Moreover, two steps were taken to simulate the focusing conditions under which the actual experiment was performed: the distance of the 57.1 cm lens from the laser was approximately the same as that of the actual focusing lens so that diffraction and beam divergence effects could be reproduced; and the lens size (≈ 10 cm diameter) was considerably larger than the beam size (about 3 mm diameter measured at the lens) so that lens aberrations

FIGURE 5

Two methods to measure beam spot size

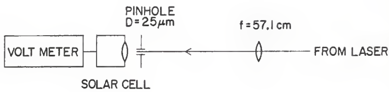

(a)

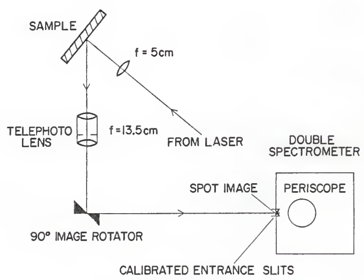

(b)

should be negligible.

Due to the fact that only the 457.9 nm radiation was used for Raman scattering purposes when the sample was heated by all-lines of the laser, it was necessary to obtain the beam spot size formed by the 457.9 nm radiation within the heating beam. This was accomplished by separating the all-line beam with a prism before focusing the 457.9 nm beam with the f=57.1 cm lens.

In addition to the spot size, data from the above mentioned measurement procedure provided the intensity distribution in the beam spot. Although small-bore lasers such as the one used in this experiment operate mostly in the TEM_{00} mode, mode mixing is not an uncommon occurrence. In fact, it was observed that the single line 488 nm beam had a doughnut shaped pattern which resembled the TEM_{10}^* mode. Such an intensity pattern is undesirable because it makes data analysis extremely difficult. However, it was found that when the laser was operating in the 514.5 nm single line and in the multi-line mode, the beam spots produced had a nice Gaussian intensity distribution. The arguments leading to such a conclusion will be discussed in the section on data reduction.

Before utilizing the data obtained in the spot size measurement procedure, the question of a small but finite size pinhole was addressed. Due to the relatively small size of the beam spot (about 120 microns diameter) even with the long focal length lens, the 25 micron pinhole sampled a relatively large area of the spot each time a power reading was taken. However, knowing the size of the circular pinhole, a sampling function could be written to unfold the experimental intensity distribution. Assuming a Gaussian intensity distribution and using the sampling function, a computer program was written to generate numbers to fit the experimental data points. This operation will be discussed fully in the data reduction section. The results showed that the intensity distributions in the beam spots measured are Gaussian.

In order to check the validity of the beam spot measurements in the first method, a second but perhaps less precise method was employed to measure the spot size when the laser was operating in the multi-line mode. Figure 5b shows the schematic for this process. Unlike the first method, the actual beam spot on the sample was magnified by a lens before its size was measured. In this method, the magnifying lens was the most important element: it must be aberration-free to produce a faithful image, and its focal length should be short in order to produce a good sized image at reasonable image distances. The Vemar Telephoto lens (f=135 mm, f/numbers from 2 to 16), which was the collection lens for the Raman signals, met the above requirements. In operation, with the "distance" control of the lens set at infinity, the lens was positioned such that the beam spot coincided with the focal point of the lens. Then adjustment was made on the "distance" control until the image of the spot was formed at the middle of the entrance slit of the SPEX double monochromator. By measuring object and image distances, the beam spot was found to be magnified by a factor of 9. The image at the entrance slits was viewed through the periscope just inside the slits after being magnified by another factor of 10 at the eyepiece. The image size was then measured by adjusting the calibrated slits of the monochromator. To ensure the least amount of lens aberration which appeared as a very "grainy" structure of the image (making estimation of the size difficult), the aperture size in the telephoto lens was decreased until the onset of diffraction effects observed as an increase in the image size at f/numbers larger than f/11. According to the diffraction formula, the diffraction limited spot size (radius) is given by:

$$r = \frac{1.22\lambda L}{D} = \frac{1.22\lambda L(f/\#)}{f} \tag{43}$$

where λ is the wavelength, L is distance from lens to the slits, D is the diameter of the aperture, f is the focal length of the lens, and f/# is the f/number of the aperture. Using the typical wavelength of 500 nm, L=135 cm as measured, f=13.5 cm, and f/#=11, r was found to be 67 microns. Compared with the image radius of 55 microns observed at the spectrometer slits, this value is a little bit large. However, considering the fact that the value of r is the distance from the image center to the first minimum of the diffraction pattern, while the observed image size was observed at the (approximate) half-power points, the measurement is reasonable. Moreover, this image radius of 55 microns translates to 6.1 microns for the real spot radius which compares very favorably with the 6.24 microns obtained by the previous method (for the all-line beam case).

It would be useful to compare the measured spot size to theoretically calculated values of the diffraction limited spot size. According to literature,[29] the TEM_{00} mode laser radiation focuses to a spot with a Gaussian radial intensity distribution at the focal plane of the focusing lens. Moreover, the diffraction-limited spot radius, if defined as the 1/e radius of the intensity distribution is given by:

$$r_s = \frac{f\lambda}{2\pi a_\ell} \tag{44}$$

where λ is the wavelength, f is the focal length of the lens, and a_ℓ is the laser beam radius at the lens. Substituting experimental values of f=5 cm, a=0.15 cm (approximate measurement with a meter stick), λ=500 nm, r_s was found to be 2.7 microns. However, it should be noted that this calculated value assumed a perfect lens and zero beam divergence, and thus represented the theoretical minimum of the spot size. In conclusion, the experimentally obtained spot sizes are reasonable values.

Signal Detection and Data Acquisition

The signal detection system consisted of a SPEX Model 1401 double monochromator with an ITT FW-130 photomultiplier tube which contained an S-20 cathode. The photomultiplier tube was thermoelectrically cooled to $-20^{o}C$ to lower the dark count to an average of 5 per second. When detecting Raman signals, both the entrance slits and the exit slits of the double monochromator were set to 200 microns, while the intermediate slits were at 500 microns to assure maximum signal throughput. With the previously mentioned collection optics, the image of the beam spot at the entrance slits was less than 40 microns in diameter although serious aberrations occurred at the focusing lens immediately in front of the entrance slits. Therefore an entrance slit size of 200 microns comfortably admitted all available signals from the sample even if slight shifts occurred in the collection optics. With the 200 micron slit settings, the resolution of the spectrometer was 4.6 cm^{-1} for the 514.5 nm laser radiation and 5.2 cm^{-1} for the 457.9 nm radiation.

A measurement of the polarization state of the Raman signals (by analyzing the signal with polarizer and polarization scrambler before entering spectrometer) showed that the intensity ratio between the horizontally polarized signal and the vertically polarized signal was exactly 2:1. It was therefore necessary to obtain the calibration of the instrumental response for the system (consisting of the collection optics, the double monochromator and the photomultiplier) for photons of both polarizations. This was done using an Electro-Optics Associates P101 standard lamp and a linear polarizer. Figure 6 shows the schematic for the calibration procedure. Spectra were taken with the polarizer in both horizontal and vertical positions. The throughput of the polarizer used was obtained by taking the spectra of a quartz-iodine lamp with one and then two (identical) polarizers in front of the spectrometer slits.

FIGURE 6

Calibration of the spectral throughput of the Raman signal collection and detection system.

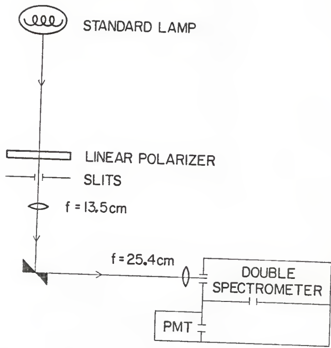
STANDARD LAMP
LINEAR POLARIZER
SLITS
f = 13.5cm
f = 25.4cm
DOUBLE
SPECTROMETER
PMT

Figure 7 is the schematic diagram of the signal detection system. Signal pulses from the photomultiplier were fed through a counting circuit consisting of a preamp, amplifier, a discriminator and time interval selector. The number of pulses counted during a selected time interval at a given spectral location was stored in a channel of the Canberra 8100A multichannel analyzer. This same information was displayed digitally on a Hewlett Packard Model 5326C frequency counter. Moreover, the rate of signal pulses was continuously monitored using a Canberra Model 1480 rate meter. At the end of a counting interval, the counting circuit provided signals to step the spectrometer to the next spectral position and to advance the channel in the multichannel analyzer. In the experiment, the Raman Stokes and anti-Stokes peaks were scanned at 2 cm^{-1} spectral increments. The counting times at each spectral position varied from 10 seconds to 20 seconds depending on the signal strength.

After a complete scan through the Raman peaks, the data stored in the multichannel analyzer were transferred to magnetic cassette tape through a Texas Instruments Silent 733 ASR data terminal. Finally, data reduction and analysis was done on a PDP-11/34 computer communicating through the TI data terminal.

Beam Chopping

It was observed in the experiment that at laser power densities of ≈1600 W/cm, extremely strong scattering of the laser beam in all directions occurred after the sample had been irradiated for about 20 minutes. This strong scattering is characteristic of sample melting as a result of increased reflectivity and surface irregularities. Moreover, at higher power levels, the time of irradiation before melting occurred was shortened. This observed behavior was unexpected because theoretical calculations[16] based on the thermal diffusivity of silicon indicated that a thermal equilibrium should be attained in a matter of microseconds. The cause

FIGURE 7

Raman signal detection system.

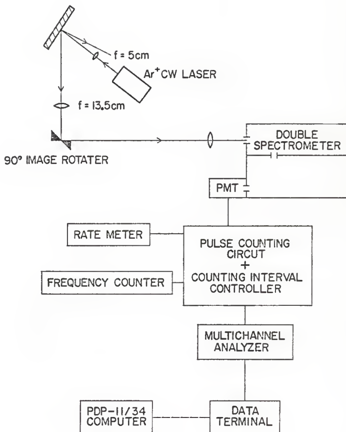
f = 5cm
Ar⁺CW LASER
f = 13.5cm
90° IMAGE ROTATER
DOUBLE
SPECTROMETER
PMT
RATE METER
PULSE COUNTING
CIRCUT
+
COUNTING INTERVAL
CONTROLLER
FREQUENCY COUNTER
MULTICHANNEL
ANALYZER
PDP-11/34
COMPUTER
DATA
TERMINAL

of this apparent long term heating degradation of the sample is not understood at this time. In order to avoid the long term heating effects, and for the fact that it took at least about 20 minutes to obtain the necessary Raman data, a chopper (25% transmittance) was put in the path of the laser beam when applying laser power (all-lines) densities at around 1600 W/cm and higher. Upon detection by a photovoltaic cell which was connected to an oscilloscope, the duration of the chopper produced laser pulses were found to be 1 msec. with 3 msec between pulses. Since it takes only microseconds to come to thermal equilibrium, the laser pulses are practically continuous in terms of heating effects. Moreover, the millisecond heating pulses simulate actual CW laser annealing of silicon in which the typical dwell time[11,13] of the scanning laser spot is in the milliseconds.

RESULTS AND ANALYSIS

As suggested in the theory and experimental sections, a number of steps must be taken to reduce the experimental data before the laser power dependence of the temperature is obtained. To find the beam spot sizes, and therefore the power density, the effect due to the finite size of the scanning pinhole needs to be removed. To extract the maximum temperature from the Raman ratio, it is necessary first to calculate the nonlinear (real) temperature profile for different possible maximum temperatures. Many of these steps involve numerical computations, mostly integrations. Fortran programs were written for these calculations. Simpson's method was used to evaluate the integrals.

One point of clarification should be mentioned. The name Raman ratio can mean either anti-Stokes to Stokes or Stokes to anti-Stokes intensity ratio. For the remainder of this thesis, the name Raman ratio specified the anti-Stokes to Stokes intensity ratio.

Absorbed Power Density

Because of the experimental arrangements, the absorbed laser power is not simply the difference between the measured incident and reflected powers. It is necessary to consider the power loss through the two focusing lenses (for the incident and reflected beams). Since the transmittance of both lenses are 95% as measured, the expression for the absorbed power is:

$$P_{abs} = 0.95P_o - \frac{P_r}{0.95} \tag{45}$$

where P_o and P_r are the measured incident and reflected power.

Figures 8 through 10 show, respectively, the measured intensity profiles obtained by the scanning pinhole method for the three beam spots produced by the single-line 514.5 nm, the 457.9 nm component of

FIGURE 8

Beam intensity profile (radial direction) produced by the single-line 514.5 nm laser beam at the focus of the 57.1 cm. lens. Solid dots are data points. Solid line is computer fit assuming an actual Gaussian intensity distribution.

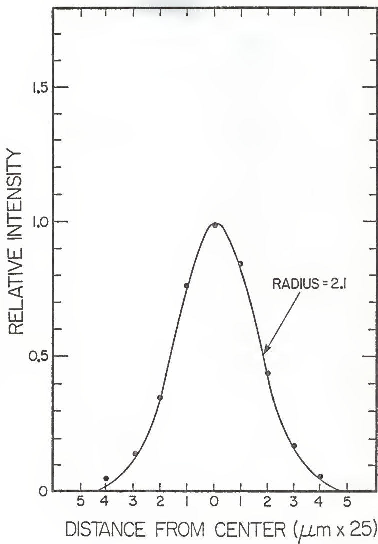
RELATIVE INTENSITY
1.5
1.0
0.5
0
RADIUS = 2.1
5 4 3 2 1 0 1 2 3 4 5
DISTANCE FROM CENTER (μm x 25)

FIGURE 9

Beam intensity profile (radial) produced by the 457.9 nm component of the multi-line laser radiation at the focus of the 57.1 cm lens. Solid line is computer fit assuming an actual Gaussian intensity distribution in the beam spot.

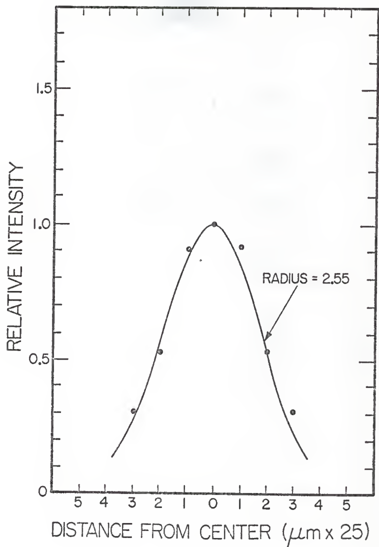
RELATIVE INTENSITY
1.5
1.0
0.5
0
RADIUS = 2.55
5 4 3 2 1 0 1 2 3 4 5
DISTANCE FROM CENTER (μm x 25)

FIGURE 10

Beam intensity profile (radial) produced by the multi-line laser radiation at the focus of the 57.1 cm lens. Solid line is computer fit assuming a Gaussian intensity distribution in the real beam spot.

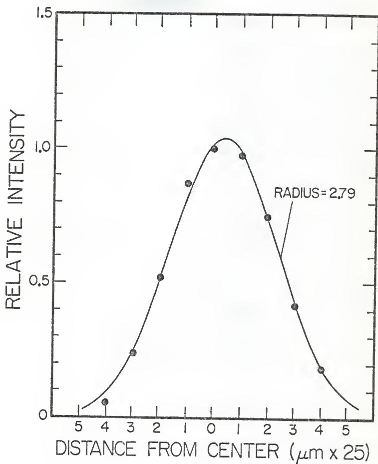
1.5
1.0
0.5
0
RELATIVE INTENSITY
RADIUS = 2.79
5 4 3 2 1 0 1 2 3 4 5
DISTANCE FROM CENTER (μm x 25)

the multi-line output, and the full multi-line laser radiations. As mentioned before, these results do not represent the actual profiles because of the size of the pinhole. Dividing the area of the pinhole into infinitesimal squares and then integrating over the circle (see appendix 2) yields the following expression that relates the experimental intensity distribution function to the real one which is assumed to be Gaussian:

$$F(Z) = \frac{1}{\sqrt{\pi}} \frac{a^2}{r^2} \int_{\frac{Z-r}{a}}^{\frac{Z+r}{a}} e^{-s^2} \operatorname{erf}\left(\frac{\sqrt{r^2-(as-Z)^2}}{a}\right) ds \qquad (46)$$

where F(Z) is the experimental intensity distribution in the radial direction Z, a is the 1/e radius of the Gaussian function, and r is the pinhole radius (=12.5 microns).

In practice, a Fortran program RADIUS (see appendix 2) was written which worked in two steps: it generated F(Z) for a given Gaussian radius a and for values of Z that correspond to the experimental points, then it calculated the sum of the square of the differences between data points and calculated points. By trial and error, the value of a which gave the least value for the sum was thus obtained. Finally, using the same program and the best value of a, a detailed curve of F(Z) was generated so that it could be plotted and compared with data. The solid lines in figures 8 through 10 are the calculated curves. The fits are generally quite good indicating that the actual intensity distributions are close to Gaussian in nature. Moreover, using the best values of a and multiplying by the ratio of focal lengths (5/57.1) as mentioned in the experimental sections, the 1/e radii of the beam spots were found to be 4.6 microns, 5.58 microns, and 6.11 microns for the single-line 514.5 nm, "multi-line" 457.9 nm and the all-line laser beams, respectively.

A word should be said about the power density. It has become customary in the literature[11] to use the power divided by the 1/e beam

radius (P/a) as the measurement of the power density of a CW laser with a radially symmetric beam profile. That it is a relevant parameter is evident in the solution to the heat transport equation. As mentioned in the theory section, the linear maximum temperature rise is given by:

$$\Theta_{max}(0,0,W) = \left(\frac{P}{a}\right) \frac{1}{2\sqrt{\pi}K_0} N(0,0,W) \quad (41)$$

where N(0,0,W) is normally a weak function of the beam radius except in cases where the beam radius is much smaller than the absorption length. Throughout our analysis, therefore, power density will correspond to the ratio of power to beam radius.

The Raman Data

Figure 11 displays the typical Raman spectra for two different absorbed powers, viz. 4.7 W/cm and 1570 W/cm. In addition to the expected relative increase in the anti-Stokes intensity in going from low to high powers, the Raman peaks are seen to broaden and become slightly asymmetric. More precisely, the shoulder of the peak is higher closer to the laser line (lower phonon frequencies) at elevated temperatures. Moreover, we observed no consistent shift in the position of the peak maxima.

Hart et al.[23] reported the line broadening and frequency shifting behavior in silicon under uniform heating up to $770^{\circ}K$. Their results indicate a phonon frequency downshift of $\simeq 2\ cm^{-1}$ per $100^{\circ}K$ increase in temperature. Bearing in mind that our Raman spectra are collections of signals from different temperature regions, it is not clear that the Raman peaks should show the same behavior. However, with the high temperature region in the spot center and with a Gaussian beam distribution (see figure 12), most of the Raman signal should come from the high temperature region. Therefore one would expect a shift in the peak position proportional to laser power. Moreover, the peaks should have a higher shoulder on the side further away from the laser line. Both these predictions were not

FIGURE 11

First-order Raman Stokes and anti-Stokes spectra of silicon for two (absorbed) power densities: 4.7 W/cm and 1570 W/cm which correspond to $300^{o}K$ (room temperature) and a peak temperature of $950^{o}K$. Note asymmetry and broadening of the Raman peaks at high temperature.

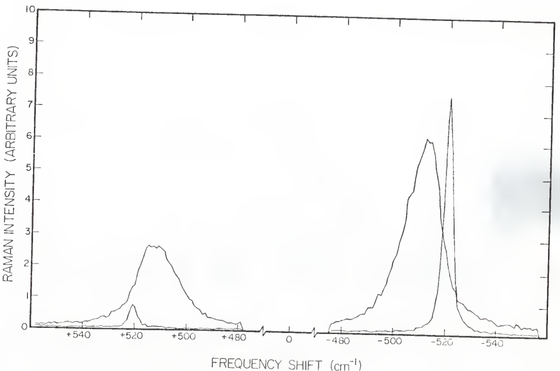
RAMAN INTENSITY (ARBITRARY UNITS)
0
1
2
3
4
5
6
7
8
9
10
+540
+520
+500
+480
0
-480
-500
-520
-540
FREQUENCY SHIFT (cm^{-1})

observed in our results.

The discrepancy between the results and predictions based on Hart's findings can perhaps be explained by the fact that a region of high pressure exists in the sample as a result of thermal expansion. Weinstein and Piermarini[31] studied the effect of hydrostatic pressure (up to 125 kbar) on the Raman spectra of silicon at room temperature. Two results of interest to us are: 1) the zone center phonon frequency increases with pressure and 2) there is no consistent and systematic pressure effect on the first-order peak intensity below about 100 kbar, which is a pressure substantially higher than the pressure that could be achieved by thermal expansion. The second result suggests that the Raman intensity ratio is not pressure dependent. On the other hand, the magnitude of the increase in the phonon frequency due to pressure can be estimated using data from the Weinstein and Piermarini article. The volume change of silicon from absolute zero to melting (1685^{0}K) is about 1.8% while the (room temperature) Grüneisen constant is ≈1 for the zone center phonon. For the phonon frequency of 519 cm^{-1} in silicon, this would mean a maximum possible frequency shift of about 10 cm^{-1}. This frequency shift will not compensate for the temperature effect (about 28 cm^{-1} shift from room temperature to melting), but it is at least a plausible explanation for the lack of large phonon shift at high temperatures. Moreover, it should be pointed out that with laser heating, the pressure on the sample is not uniform in all directions. In fact, the radially symmetric stress in our case resembles the uniaxial stress which has been shown to produce a splitting in the triply degenerate optical phonon.[32] This effect, combined with the pressure variations in the sample due to a temperature gradient, makes analysis of the Raman lineshape and peak frequency very difficult.

With all the above considerations, it is not likely that the Raman ratio can be accurately represented by the ratio of the peak heights. An integration over the peaks before calculating the ratio would be

more reasonable. Moreover, such a procedure can reduce the statistical uncertainties in the measurements. In practice, the peaks were integrated between the half-maximum points. The background counts were obtained by summing over 10 channels (20 cm^{-1}) on either side of the peaks and then averaging.

Corrections For Instrumental Efficiency

Instrumental efficiency correction was applied to the experimental Raman ratios so that the actual ratio from the sample could be obtained. As mentioned in the experimental section, the ratio of the number of horizontally polarized photons to vertically polarized photons is 2:1. Therefore, the real Raman ratio is given by (see appendix 3):

$$R = R_o \left(\frac{2H_S+V_S}{2H_A+V_A}\right) \tag{47}$$

where R_o is the ratio before the correction; H,V correspond to the instrumental efficiency for horizontally and vertically polarized radiation, respectively; the subscripts A and S denote the quantity being at the anti-Stokes or Stokes frequency.

The following table shows experimental values of H_S, V_S, H_A, V_A for Raman excitation wavelengths 457.9 nm and 514.5 nm and for the phonon wavenumber 519 cm^{-1}:

	H_A	V_A	H_S	V_S
457.9nm	8.61	6.98	8.19	6.98
514.5nm	7.83	6.14	6.63	6.12

Substituting these numbers into equation (48) results in instrumental correction factors for the 457.9 nm and 514.5 nm excited Raman ratios as 0.965 and 0.889 respectively.

The ω^3 Correction

As discussed in the theory section, the Raman ratio in terms of number of photons is proportional to the ratio of the scattered photon frequencies raised to the third power. This ω^3 factor is a fixed number for a given Raman excitation frequency, and can be viewed as a correction factor for the Raman ratio:

$$R_{corr} = \left(\frac{\omega_i - \Omega}{\omega_i + \Omega} \right)^3 R = \frac{n_o}{n_o + 1} \tag{48}$$

where the notations are the same as were used in the theory section.

The calculation of R_{corr} is the last step in the manipulation of the experimental Raman data. The rest of the data reduction process involves the generation of a maximum temperature vs. R_{corr} curve using the theoretically calculated temperature profiles and the previously obtained beam spot sizes.

Raman Ratio as a Function of Peak Temperature

The previously obtained equation for the Raman ratio must be revised due to variations in temperature in the region where Raman scattering occurs. Variations in temperature affect the phonon distribution n_o. Assuming that the temperature is known as a function of position, the phonon distribution function is known everywhere. With the cylindrical symmetry of the problem, the Raman intensity (in number of photons) can be written as an integral of signals from rings of radius r and thickness dz on the sample:

$$N_{anti\text{-}Stokes} \propto \omega_{AS}^3 \int_0^\infty e^{-(\alpha_L + \alpha_{AS})z}\, dz \int_0^\infty n_o\, e^{-\frac{r^2}{a^2}} (2\pi r) dr \tag{49}$$

$$N_{Stokes} \propto \omega_S^3 \int_0^\infty e^{-(\alpha_L + \alpha_{AS})z}\, dz \int_0^\infty (n_o + 1) e^{-\frac{r^2}{a^2}} (2\pi r) dr \tag{50}$$

where α_L, α_{AS}, α_S are the absorption constants at the Raman excitation frequency, the anti-Stokes frequency, and the Stokes frequency respectively; a is the beam spot radius. The factors $(\alpha_L + \alpha_{AS})$ and $(\alpha_L + \alpha_S)$ account for

the absorption experienced by the incident and scattered photons. Assuming negligible change in the absorption constant in going from the Stokes to anti-Stokes frequency, both $(\alpha_L+\alpha_{AS})$ and $(\alpha_L+\alpha_S)$ are approximately equal to $2\alpha_L$. Converting to dimensionless variables by using a as a length unit as was done in the theory section, the corrected Raman ratio can best be expressed in the inverse form:

$$\frac{1}{R_{corr}} = 1 + \frac{\int_0^\infty e^{-2W_L Z}\, dZ \int_0^\infty e^{-R^2}\, RdR}{\int_0^\infty e^{-2W_L Z}\, dZ \int_0^\infty n_0 Re^{-R^2}\, dR} \qquad (52)$$

Here the population factor n_0 for a given maximum temperature (temperature at spot center) can be found for all positions by using equations derived by Lax, which contain an integral. The expression for R_{corr} therefore involves triple integrals. To carry out such calculations would require extremely long running time on the computer plus the possibility of inadequate numerical accuracy as a result of truncation errors and limited increments for the integrations. However, it was observed that the integration in the z direction should contribute very little to the Raman ratio because of the small absorption length in silicon. To illustrate this point, figure 12 shows the temperature profile together with the Raman beam irradiance $e^{-\alpha_L Z}$ in the z-direction for the multi-line heating case (W=7.6). The temperature profile (at R=0) is for a peak temperature of 1300°K and is calculated using equations of Lax:

$$N(R,Z,W) = \frac{W}{\sqrt{\pi}} \int_0^\infty J_0(\lambda R) e^{-\frac{1}{4}\lambda^2} \frac{We^{-\lambda Z} - \lambda e^{-WZ}}{W^2 - \lambda^2}\, d\lambda \qquad (42)$$

and subsequent conversion to real temperatures (see Appendix 4 for program TEMPRZ). The absorption constant α for the 457.9 nm Raman radiation is $2.08 \times 10^4\ cm^{-1}$ from Dash and Newman.[28] Compared with the temperature profile, it can be seen that the beam irradiance is an extremely sensitive

FIGURE 12

Calculated temperature profiles and beam irradiance (dashed lines) profiles in the radial and longitudinal (z) directions for the multi-line heating case (W=7.6) and for a peak temperature of 1300°K. The irradiance profile in the z direction is for the 457.9 nm Raman radiation.

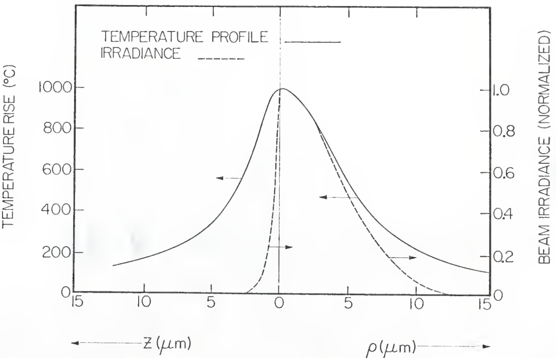
TEMPERATURE PROFILE
IRRADIANCE
TEMPERATURE RISE (°C)
1000
800
600
400
200
0
BEAM IRRADIANCE (NORMALIZED)
1.0
0.8
0.6
0.4
0.2
0
15
10
5
0
5
10
15
z (μm)
ρ (μm)

function of z. Therefore the integration in the z-direction can be de-coupled from the radial integral. Moreover, the Raman radiation samples only the region very close to the surface. Consequently, the population factor $n_o(R,Z)$ can be approximated by $n_o(R,0)$ in the radial integral. The expression for the Raman ratio becomes:

$$\frac{1}{R_{corr}} = 1 + \frac{1}{2}\left[\int_o^\infty n_o(R,0)Re^{-R^2}\,dR\right]^{-1} \tag{52}$$

To obtain the Raman ratio as a function of peak temperature, the following procedure was taken: 1) the linear temperature profile was calculated, 2) real temperature profiles T(R,0) were obtained for different peak temperatures, and 3) knowing T(R), the phonon distribution factor $n_o(R)$ was known, and therefore R_{corr} was obtained by performing the integration over R. In practice, three programs were written to carry out these steps. The program TEMPR (appendix 5) calculated the normalized linear temperature N(R,Z,W) with Z=0:

$$N(R,0,W) = \frac{W}{\sqrt{\pi}}\int_o^\infty \frac{J_o(\lambda R)\,e^{-\frac{1}{4}\lambda^2}}{W+\lambda}\,d\lambda \tag{53}$$

A total of 51 points were obtained for N(R) between R=0 and 3 at increments of 0.06 in anticipation of the following integral. The limit R=3 is sufficient although theoretically R should go to infinity because it can be shown that for a Gaussian beam, the circular area of radius 3a (a is 1/e radius) contains 99.987% of the total power while the population n_o increases by less than a factor of 2 going from room temperature to melting. On the other hand, the R-increments of 0.06 was chosen because integrations (in the following radial integration) with half as many divisions in R (increments of 0.12) showed essentially no significant loss in accuracy (the results agree to within 0.5% of the more accurate results).

The second program TTEMPR (appendix 6) produces the real temperature as a function of R for each maximum temperature (at R=0). It worked in two steps: 1) N(R) from the first result was renormalized to a maximum linear temperature that corresponds to a real peak temperature in question, and 2) the linear temperature profiles were converted to the real temperature profiles in a point by point conversion process. The conversion curve, which was previously calculated from thermal conductivity data, consisted of 43 points ranging from room temperature to the melting point. Linear interpolation was used in the conversion process. Thus 28 temperature profiles corresponding to 28 peak temperatures ranging from 300°K to 1650°K at 50°K increments were produced for each beam radius.

Once the temperature profiles are known, the Raman ratio vs. maximum (peak) temperature curve can be calculated. Program RATIO2 (appendix 7) was written for this calculation, which is essentially the integration process with the integration limits for R being zero and 3 as discussed above. Care was taken to account for the difference in spot size between the heat beam and the Raman probe when the laser was operating in the multi-line mode. A simple change was made to equation (52) for the Raman ratio to this effect:

$$\frac{1}{R_{corr}} = 1 + \frac{1}{2\beta^2}\left[\int_0^\infty n_o R e^{-R^2\beta^2} dR\right]^{-1} \tag{54}$$

Here β is the ratio of the heat beam radius to the Raman probe beam radius. Using experimental values of 6.11 and 5.58 microns (see section on absorbed power density), β is 1.095 for the multi-line heating case. In the case of single-line laser heating (514.5 nm), β was set to 1. Figure 13 shows the resulting curves of Raman ratio vs. peak temperature for the single-line and multi-line heating cases.

Peak Temperature as a Function of Power Density

Using the Raman ratio vs. peak temperature curves and the experimental values of R_{corr}, the relation between absorbed power density and peak temperature was obtained. The results are shown in figure 14. Instead of

FIGURE 13

Calculated curves of the Raman ratio as a function of peak temperature. The lower curve is for the single-line 514.5 nm case (W=4.6). The upper curve is for the multi-line heating case (W=7.6) with the 457.9 nm Raman excitation.

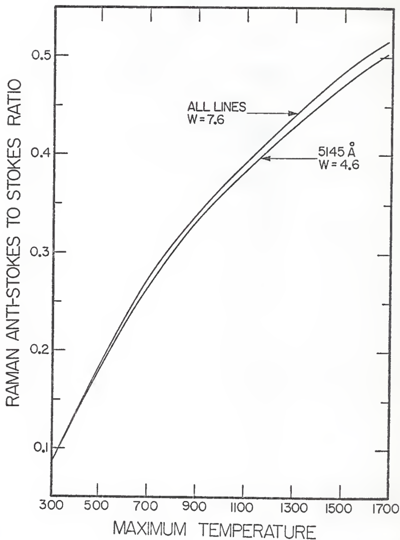
RAMAN ANTI-STOKES TO STOKES RATIO
0.5
0.4
0.3
0.2
0.1
ALL LINES
W = 7.6
5145 Å
W = 4.6
300
500
700
900
1100
1300
1500
1700
MAXIMUM TEMPERATURE

FIGURE 14

Peak temperature as a function of power density. The open circles represent experimental data taken with single-line 514.5 nm beam. The triangles represent experimental data taken with the multi-line heating beam and with the 457.9 nm Raman excitation. The cross represents minimum power density that produced sample melting. The solid curves are theoretical (nonlinear) results assuming a constant room temperature absorption constant. The dashed curve is the theoretical results for $W \to \infty$. All the multi-line data points at 1600 W/cm and higher power levels were taken with chopper in laser beam.

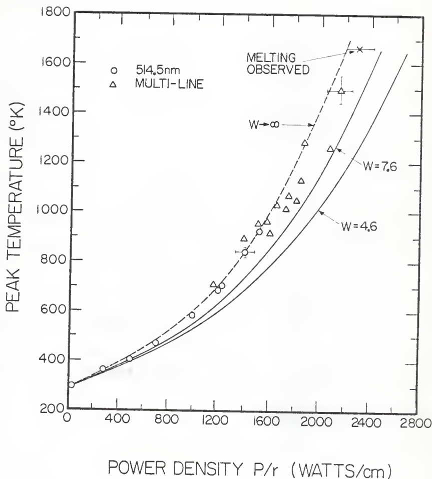

PEAK TEMPERATURE (°K)
1800
1600
1400
1200
1000
800
600
400
200
0
400
800
1200
1600
2000
2400
2800
514.5nm
MULTI-LINE
MELTING OBSERVED
W→∞
W=7.6
W=4.6
POWER DENSITY P/r (WATTS/cm)

reading off values from the ratio vs. temperature curves, a program RTCONV (see appendix 8) was written using linear interpolation to convert R_{corr} into temperature. Representative error bars were put on two sets of data points. The error estimates were made based on the statistical fluctuations in the photon counts and on the precision of the power measurements and spot size determinations.

In addition to the temperatures obtained through Raman ratios, we also obtained experimentally the power needed to melt the sample under milti-line laser radiation (see figure 14). The power of the laser was very slowly increased (chopper in beam) until the sample started to melt which could easily be identified as a sudden and extremely strong scattering of the laser radiation in all directions. This change in the scattering pattern is expected for two reasons: 1) the sample surface becomes irregular as it melts and 2) the reflectivity of the sample undergoes a rise as it becomes liquid.

For comparison, the peak temperatures predicted by calculations using Lax's equations are also shown in figure 14. Since the linear profile N(R,0,W) was already found in the previous process of data reduction, it was most convenient to express the linear maximum temperature $\Theta(0,0,W)$ as:

$$\Theta(0,0,W) = \left(\frac{P}{a}\right) \frac{1}{2\sqrt{\pi}K_0} N(0,0,W) \tag{41}$$

where P/a is the power density. A program TPOWD (appendix 9) was written which used the linear to nonlinear temperature conversion curve and the above equation to generate the theoretical curves.

Despite some scattering in the data points, it is clear from figure 14 that the experimental points fall consistently above the theoretical predictions. In an attempt to explain the differences, we analyzed possible systematic errors in the experimental data, namely the power density measurements and the Raman measurements. The data

point obtained by direct observation of the melting power density of the sample falls in line with the other data points and, since it is a direct observation, gives strong support to the Raman temperature measurements. On the other hand, in order to force the experimental points to fit the theoretical curves, the beam spot radii must be reduced by roughly 20%. For the case of a 4.6 microns radius, it must be reduced to 3.7 microns. In addition to the fact that the spot sizes are measured and double checked with two different methods, it is unlikely that a spot radius of 3.7 microns can be obtained for the following reason. According to estimates discussed in the experimental section, the minimum value for the radius is 2.7 microns assuming perfect lens and zero laser beam divergence, both of which are unrealistic conditions. Consequently, no reasonable systematic adjustments can be made to the experimental data.

Turning to the theoretical calculations and the underlying assumptions and approximations which were discussed in detail in the theory section, it is readily seen that the assumption of a fixed absorption constant cannot be applied to the case of silicon. However, since we are not aware of any experimental data on the high temperature dependence of the absorption constant α in silicon, it is impossible to construct a realistic theoretical temperature vs. power density curve. On the other hand, it is possible to establish some guidelines towards the behavior of the absorption constant at higher temperatures. According to Oash and Newman[28], the energy band gap in silicon decreases at a rate of roughly 5×10^{-4} eV/^{o}K between the temperatures 77°K and 300°K. Moreover, the absorption constant vs. photon energy curves for the two temperatures are approximately parallel. Assuming that such behavior continues into the high temperature regions, the absorption constant can be found by a horizontal displacement of the curve corresponding to the amount of

shift in the band gap. For a temperature rise of $1000^{0}K$ and for the photon energy of 2.5 eV (the average energy of the multi-line Ar^{+} laser photon), the absorption constant is found to increase by a factor of 4 from the room temperature value. The value of W (defined as α times the spot radius) therefore changes from 7.6 to 30 in the case of the multi-line radiation. As mentioned in the theory section, the behavior of the linear beam profile N(0,0,W) approaches the limiting behavior ($W\to\infty$) at these W values. Recalling the expression for the maximum linear temperature:

$$\Theta(0,0,W) = \left(\frac{P}{a}\right) \frac{1}{2\sqrt{\pi}K_0} N(0,0,W) \xrightarrow{W\to\infty} \left(\frac{P}{a}\right) \frac{1}{2\sqrt{\pi}K_0} \tag{41}$$

This equation therefore provides a more realistic temperature vs. power density curve in the high temperature regions.

On the other hand, an increase in the absorption constant can also affect the peak temperatures derived from the Raman ratios. To determine the extent of the change, a Raman ratio vs. peak temperature curve was developed for W=30. The results are displayed in Table 1 together with W=7.6 values for comparison purposes. It can be seen that for the same peak temperature, the maximum change in the Raman ratio in going from W=7.6 to W=30 is less than 2% producing an upshift in temperature of less than $40^{0}K$ at the highest temperature data points. The shift should be much smaller for the lower temperature data points although the exact amount is not known because of a lack of absorption constant data. Since the shifts in the temperatures are not large compared with the experimental uncertainties, no attempt was made to move the data points to suit higher absorption constants.

The theoretical temperature vs. power density curve for the limiting values of W is also shown in figure 14. As expected, this curve gives much better fit to the data for high temperatures. However, it can be seen that even for the lower temperature 514.5 nm data, the fit is very

TABLE 1

Calculated Raman ratios as a function of peak temperature for the two cases: W=30 and W=7.6.

TEMPERATURE	RATIO1 (W=30)	RATIO2 (W=7.6)
300	0.0828345	0.0828345
350	0.1094267	0.1100227
400	0.1348507	0.1360399
450	0.1596565	0.1614699
500	0.1830201	0.1853900
550	0.2057453	0.2086637
600	0.2278999	0.2313934
650	0.2490528	0.2530552
700	0.2688010	0.2732493
750	0.2870883	0.2919479
800	0.3040906	0.3092829
850	0.3202268	0.3257564
900	0.3354493	0.3412940
950	0.3499496	0.3560417
1000	0.3635984	0.3700564
1050	0.3767003	0.3833349
1100	0.3893364	0.3962237
1150	0.4014407	0.4084688
1200	0.4129629	0.4202725
1250	0.4243554	0.4317749
1300	0.4354899	0.4430408
1350	0.4462137	0.4540183
1400	0.4567428	0.4646397
1450	0.4670283	0.4749317
1500	0.4770064	0.4851243
1550	0.4867728	0.4949638
1600	0.4962720	0.5045550
1650	0.5055330	0.5138918

good. This behavior is unexpected because with the gradual increase of the absorption constant, the temperature curve should rise gradually from the W=4.6 curve into the limiting curve. The cause of this behavior is not understood, although one possible factor is the uncertainty in the room temperature thermal conductivity value which is believed to be accurate only to within 5%. Since the calculated temperature is directly proportional to the inverse of this thermal conductivity value, the uncertainty in the entire theoretical curve is also 5%.

SUMMARY AND CONCLUSIONS

The Raman technique has been shown to be a feasible way to measure sample temperature during heating of pure silicon by a Gaussian beam. In conjunction with theoretically calculated temperature gradients, it was shown that the Raman ratio can be used to extract the temperature rise. Uncertainties in the calculated temperature gradients are not critical because the resulting maximum temperature derived from the Raman data is insensitive to small errors in the temperature gradient. Of course, no theoretical calculations would need be invoked in the Raman method of temperature measurement if one had available large heated areas that allow for the use of a small, low-powered Raman probe beam. On the other hand, we have shown that in silicon, temperature variations in the absorption constant cannot be neglected in theoretical calculations of the temperature rise. Moreover, the data show that the closed-form solutions of the nonlinear heat conduction equation proposed by Lax do provide a way to predict accurately the temperature rise in the case of large absorption constants and large beam spot sizes.

With the confirmation of the Raman temperature measurement technique in pure silicon samples, the next step would be temperature measurements in ion-implanted samples during laser annealing. Here the technique would be clearly superior to theoretical calculations because the Raman technique will not be affected by subtle uncertainties in the properties of the material such as absorption constant and thermal conductivity. Moreover, the theoretical calculations do not account for the heat of recrystallization which is released as the damaged silicon changes into single crystal material during laser annealing.

Future experiments have also been planned to extend the Raman technique to temperature measurements during pulsed laser annealing. With adequate instrumentation such as a silicon intensified target (SIT)

detector that can detect the entire Raman spectrum at the same time, and using a time-delayed Raman probe beam, it should be possible to obtain a time-resolved temperature profile which traces the temperature during and after the application of the heating laser pulse. It is hoped that the experience gained in this present study will help in the progress of the planned experiments and in the understanding of the basic mechanisms of the laser annealing process.

APPENDIX 1

Program TCONV

The Fortran program TCONV computes the linear temperature rise (above room temperature) as a function of the nonlinear temperature T following equation of Lax:

$$\Theta(T) \equiv \int_{T_o}^{T} \frac{K(T)}{K_o}\, dT \tag{20}$$

The thermal conductivity values are taken from C.Y. Ho et al.[25].

Following is the program listing for TCONV.

```
C
C THIS PROGRAM CALCULATES LINEAR TEMP RISE AS A FUNCTION
C OF NONLINEAR TEMP
C EQUATION OF M. LAX IS USED
C SIMPSON'S METHOD USED FOR INTEGRATION
C
C INPUT IS DATA FILE(COND.DAT) CONTAINING THERMAL
C CONDUCTIVITY VALUES FROM ROOM TEMP TO 1675K
C AT 25 DEGREE INTERVALS
C
C OUTPUT VALUES AS FOLLOWS:
C T = NONLINEAR TEMP FROM 350K TO 1650K AT 50 DEGREE INTERVALS
C RTEMP = CORRESPONDING LINEAR TEMP RISE ABOVE 300K
C
C
      DIMENSION Y(56)
      OPEN (UNIT=3,NAME='DK:COND.DAT',TYPE='OLD')
      READ (3,100) (Y(I),I=1,56)
100   FORMAT (10F6.3)
      H=25.
      T=350.
      SUM=Y(1)+4*Y(2)+Y(3)
      I=1
C
C 3*1.48(ROOM TEMP CONDUCTIVITY)=4.44
C
11    RTEMP=(H*SUM)/4.44
      TYPE 200,T,RTEMP
200   FORMAT(2F16.7)
      IF(T .GE. 1650.) GO TO 22
      T=T+50.
      I=I+2
      SUM=SUM+Y(I)+4*Y(I+1)+Y(I+2)
      GO TO 11
22    CONTINUE
      STOP
      END
```

APPENDIX 2

Effect of Pinhole on the Observed Intensity in Beam Spot

The observed intensity is a collection of radiation coming through the pinhole. Figure 15 shows the geometry of the set-up. The pinhole moves on a line described by OO', the beam spot center and the center of the pinhole. Dividing the pinhole (radius r) into infinitesimal squares of area dA=dydx, and assuming a Gaussian intensity distribution in the beam spot (1/e radius = a), the relative intensity F(Z) observed with pinhole at a distance Z from the beam center can be found by an integration over the area of the pinhole

$$F(Z) = \frac{1}{\pi r^2} \iint_{\text{pinhole}} e^{-\left(\frac{\sqrt{(Z+X)^2+y^2}}{a}\right)^2} dydx = \frac{2}{\pi r^2} \int_{-r}^{+r} e^{-\left(\frac{Z+X}{a}\right)^2} dx \int_0^{\sqrt{r^2-x^2}} e^{-\left(\frac{y}{a}\right)^2} dy$$

The y-integral can be represented by the error function. Putting the integral into the form of the error function with a change of variable t=y/a:

$$F(Z) = \frac{2}{\pi r^2} \frac{\sqrt{\pi}}{2} a \int_{-r}^{+r} e^{-\left(\frac{Z+X}{a}\right)^2} dx \frac{2}{\sqrt{\pi}} \int_0^{\frac{1}{a}\sqrt{r^2-x^2}} e^{-t^2} dt$$

$$= \frac{1}{\sqrt{\pi}} \frac{a}{r^2} \int_{-r}^{+r} e^{-\left(\frac{Z+X}{a}\right)^2} \operatorname{erf}\left(\frac{1}{a}\sqrt{r^2-x^2}\right) dx$$

Finally, a further change of variables s=(Z+x)/a yields the more symmetric expression for the observed intensity:

$$F(Z) = \frac{1}{\sqrt{\pi}} \left(\frac{a}{r}\right)^2 \int_{\frac{Z-r}{a}}^{\frac{Z+r}{a}} e^{-s^2} \operatorname{erf}\left(\frac{\sqrt{r^2-(as-Z)^2}}{a}\right) ds$$

The Fortran program RADIUS was written to perform the computation of F(Z). The listing follows.

FIGURE 15

Geometry of pinhole in the beam spot

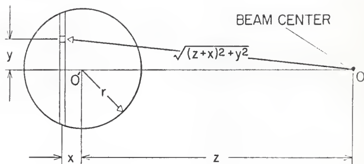
BEAM CENTER
y
O'
r
$\sqrt{(z+x)^2+y^2}$
O
x
z

```
RADIUS
C THIS PROGRAM UNFOLDS THE GAUSSIAN PROFILE SAMPLED BY A
C     SMALL BUT FINITE SIZE CIRCULAR AREA
C THE RESULTING FUNCTION FOR A GIVEN GAUSSIAN RADIUS IS FITTED
C     TO DATA
C OUTPUT: UNFOLDED FUNCTION AND SUM OF SQUARES
C INPUT AS FOLLOWS:
C N = NUMBER OF DATA POINTS
C ARRAY DATA(I) IS ARRAY OF DATA POINTS;NORMALIZED WITH MAXIMUM
C     VALUE=1
C W = 1/E RADIUS OF THE GAUSSIAN FUNCTION IN UNITS OF 25 MICRONS
C R = PINHOLE RADIUS IN UNITS OF 25 MICRONS
C FNOR = NORMALIZATION FACTOR FOR THE FIT CURVE TO ALLOW
C         FOR VARIATIONS IN THE PEAK INTENSITY
C ZMAX,ZMIN,ZINC ARE MAXIMUM AND MINIMUM Z AND Z INCREMENT
C  FOR Z VALUES TO MATCH THOSE OF THE DATA. SLIGHT VARIATIONS
C  IN ZMAX AND ZMIN CAN SHIFT THE LOCATION OF THE PEAK TO
C  OBTAIN THE BEST FIT TO THE DATA POINTS
C ALL THE LENGTH VALUES IN THE PROGRAM ARE IN UNITS
C  OF 25 MICRONS
C NI = MINIMUM NUMBER OF DIVISIONS IN THE INTEGRATION
C THE NUMBER OF DIVISIONS FOR INTEGRATION IS INCREASED (DOUBLED)
C  UNTIL TWO CONSECUTIVE INTEGRATIONS AGREE TO 0.0001
C
C
        DIMENSION DATA(20),FIT(20),TI(10)
        LOGICAL*1 A(15),C,D,E
C
C F(S) IS THE INTEGRAND
C
        F(S)=ERF(SQRT(R*R-(W*S-Z)**2)/W)/EXP(S*S)
        CALL PRINT ('TYPE IN DATA FILENAME,DK:FILNAM.TYP')
        ACCEPT 100,A
100     FORMAT(15A1)
        OPEN(UNIT=1,NAME=A,TYPE='OLD')
        READ(1,200) N,(DATA(I),I=1,N)
200     FORMAT(I2/(10F6.3))
        CALL PRINT('TYPE MAXZ,MINZ AND ZINC IN F6.3')
        ACCEPT 300,ZMAX,ZMIN,ZINC
300     FORMAT(3F6.3)
555     CALL PRINT('GAUSSIAN RADIUS PARAMETER FIT=?')
        ACCEPT 400,W
400     FORMAT(F16.7)
        CALL PRINT('PINHOLE RADIUS=?')
        ACCEPT 123,R
123     FORMAT(F16.7)
        CALL PRINT('MINIMUM NUMBER OF DIVISIONS FOR INTEGRATION=?')
        ACCEPT 456,NI
456     FORMAT(I4)
        CALL PRINT('PEAK OF FIT CURVE NORMALIZED TO?')
        ACCEPT 797,FNOR
797     FORMAT(F5.3)
        TYPE 333
333     FORMAT(' $WANT CALCULATED NUMBERS?')
```

```
        ACCEPT 800,E
        IF(E .NE. 'Y')GO TO 334
        TYPE 450
450     FORMAT(' ',8X,'Z',15X,'FIT',9X,'I',3X,'IN',6X,'R',9X,'W')
334     ZZ=ZMIN
        NH=N+1
        DO 1 I=1,NH
C
C DO INTEGRATION FOR EACH Z
C
        Z=ABS(ZZ)
        IF(I .EQ. NH) Z=0.0
        FNI=NI
C
C DIFFERENCE BETWEEN INT LIMITS IS 2R/W
C
        B1=(Z-R)/W
        B2=(Z+R)/W
        DO 5 M=1,10
        IN=IFIX(FNI+0.5)
        H=2*R/(W*FNI)
        TWOH=H+H
11      SUM4=0.0
        SUM2=0.0
        S=B1+H
        J=1
21      SUM4=SUM4+F(S)
        SUM2=SUM2+F(S+H)
        IF(J .GE. IN-3) GO TO 31
        J=J+2
        S=S+TWOH
        GO TO 21
C
C INVERSE OF SQRT(PI) = 0.56418958
C
31      TI(M)=0.56418958*(W*W)/(R*R)*(H/3.0)*(4.0*SUM4+2.0*SUM2
     1+4.0*F(B2-H))
        FNI=FNI*2.0
        IF(M .EQ. 1) GO TO 5
        M1=M
        M2=M-1
        IF(TI(M)-TI(M2) .LE. 0.0001) GO TO 41
5       CONTINUE
C
C GENERATE FIT CURVE
C
41      FIT(I)=TI(M1)
        IF(E .NE. 'Y') GO TO 335
        TYPE 600,Z,FIT(I),I,IN,R,W
600     FORMAT(' ',2F16.7,I5,I6,2F10.3)
335     ZZ=ZZ+ZINC
1       CONTINUE
```

```
C
C NORMALIZE CURVE TO PEAK=FNOR
C
        FMAX=FIT(NH)
        DO 15 I=1,N
15      FIT(I)=FIT(I)/FMAX*FNOR
C
C CALCULATE SUM OF SQUARES
        SUM=0.0
        DO 3 I=1,N
3       SUM=SUM+(DATA(I)-FIT(I))**2
        TYPE 710,SUM
710     FORMAT(' ','SUM OF SQUARES=',E16.7)
        TYPE 144
144     FORMAT('$WANT NORMALIZED FIT?')
        ACCEPT 800,D
        IF(D .NE. 'Y') GO TO 245
        TYPE 913
913     FORMAT(' ',8X,'Z',11X,'NORMALIZED FIT')
        Z=ZMIN
        DO 16 I=1,N
        TYPE 914,Z,FIT(I)
16      Z=Z+ZINC
914     FORMAT(' ',2F16.7)
245     TYPE 158
158     FORMAT('$TRY AGAIN?')
        ACCEPT 800,C
800     FORMAT(A1)
        IF(C .EQ. 'Y') GO TO 555
        STOP
        END
        FUNCTION ERF(SX)
C THIS PROGRAM CALCULATES ERROR FUNCTION OF X IN DOUBLE PRECISION
C OUTPUT IS SINGLE PRECISION
C NORMALIZATION FACTOR IS 2/SQRT(PI)
C INTEGRATION LIMIT IS ZERO TO X
        DOUBLE PRECISION X,Z,T
        X=DBLE(SX)
        T=1.0/(1.0+0.3275911*X)
        Z=DLOG(0.254829592*T-0.284496736*T**2+1.421413741*T**3
     1  -1.453152027*T**4+1.061405429*T**5)-X*X
        ERF=SNGL(1.0-DEXP(Z))
        RETURN
        END
```

APPENDIX 3

Instrumental Efficiency Correction to the Raman Ratio: Polarized Radiation

In the experiment it was observed that the ratio of number of photons polarized in the horizontal direction to that in the vertical direction is 2:1. Therefore if h is the number of horizontally polarized Raman photons, and v is the vertical component emitted by the sample per unit time, then h=2v. The number of Raman photons N detected by the spectrometer per unit time is given by

$$N = Hh + Vv = v(2H+V)$$

where H and V are the instrumental efficiencies for the horizontally and vertically polarized photons. Then the real Raman ratio R is given by

$$R = \frac{N_A}{2H_A+V_A} \cdot \frac{2H_s+V_s}{N_s} = \left(\frac{2H_s+V_s}{2H_A+V_A} \right) R_o$$

where $R_o = N_A/N_S$ is the Raman ratio as detected by the spectrometer. The subscripts A and S for N refer to the anti-Stokes and Stokes components; while H_A and V_A are the instrumental efficiencies for the horizontally and vertically polarized radiation at anti-Stokes frequency. Similarly, H_S and V_S are the quantities at the Stokes frequency.

APPENDIX 4

Program TEMPRZ

The Fortran program TEMPRZ was used to compute the linear temperature profiles in both the radial and longitudinal directions. Calculations are based on the equation by Lax:

$$N(R,Z,W) = \frac{W}{\sqrt{\pi}} \int_0^\infty J_0(\lambda R) e^{-\frac{1}{4}\lambda^2} \frac{We^{-\lambda Z} - \lambda e^{-WZ}}{W^2 - \lambda^2} \, d\lambda \tag{42}$$

The zeroth order Bessel function is evaluated using a polynomial approximation.[32]

```
TEMPRZ
C
C THIS PROGRAM CALCULATES LINEAR TEMP PROFILES N(R,Z,W)
C M. LAX'S EQUATIONS ARE USED
C
C OUTPUT IS DATA FILE 'TPROF2.DAT' WHICH CONTAINS AN ARRAY IN
C   TWO DIMENSIONS REPRESENTING R AND Z
C
C INPUT AS FOLLOWS:
C R2 = MAXIMUM VALUE OF R IN N(R,Z,W)
C Z2 = MAXIMUM VALUE OF Z IN N(R,Z,W)
C MR = NUMBER OF R VALUES IN N(R,Z,W) EVALUATED
C MZ = NUMBER OF Z VALUES IN N(R,Z,W) EVALUATED
C  W = PRODUCT OF 1/E BEAM RADIUS AND ABSORPTION CONSTANT
C  N = NUMBER OF DIVISIONS USED IN THE INTEGRATION (SIMPSON'S RULE)
C
C ALL R,Z VALUES ARE IN UNITS OF THE BEAM RADIUS
C IN THIS PROGRAM THE UPPER LIMIT OF INTEGRATION IS SET AT 10
C
C
      DIMENSION STRING(41,51)
C
C F(Y) IS INTEGRAND
      F(Y)=BESS(Y*R)*(W/EXP(Y*Z)-Y/EXP(W*Z))/(EXP(Y*Y/4.)*(W*W-Y*Y))
      TYPE 500
500   FORMAT(/  TYPE IN THE FOLLOWING VALUES:'/
     1' MAXIMUM VALUE FOR R IS')
      ACCEPT 510,R2
510   FORMAT(F4.1)
      TYPE 600
600   FORMAT(/' NUMBER OF DIVISIONS FOR INTEGRATION IN R IS:')
      ACCEPT 520,N
520   FORMAT(I3)
      TYPE 700
700   FORMAT(/' VALUE OF BEAM WAIST RADIUS IS :')
      ACCEPT 510,W
      TYPE 800
800   FORMAT(/' MAXIMUM VALUE OF Z IS :')
      ACCEPT 510,Z2
      TYPE 1000
1000  FORMAT(/' NUMBER OF POINTS IN R IS :')
      ACCEPT 520,MR
      TYPE 1100
1100  FORMAT (/' NUMBER OF POINTS IN Z IS :')
      ACCEPT 520,MZ
      Z=0.0
      FMZ=MZ-1
      FMR=MR-1
      RINC=R2/FMR
      ZINC=Z2/FMZ
      DO 51 K=1,MZ
      VMAX=10.0
      VMIN=0.0
      FN=N
      H=VMAX/FN
      TWOH=H+H
```

```
      P=0.0
      J=1
1     SUM4=0.0
      SUM2=0.0
      X=H
      I=1
2     SUM4=SUM4+F(X)
      SUM2=SUM2+F(X+H)
      IF(I.GE.N-3) GO TO 3
      I=I+2
      X=X+TWOH
      GO TO 2
C
C SQUARE ROOT OF PI = 1.7724539
3     TEMPN=W*H/3.0*(4.0*SUM4+2.0*SUM2+F(VMIN)+4.0*F(VMAX-H)
     1+F(VMAX))/1.7724539
      STRING(K,J)=TEMPN
      J=J+1
      P=P+PINC
      IF(P.LE.P2) GO TO 1
      TYPE 11,Z,P,TEMPN
11    FORMAT(1X,3F16.7)
      Z=Z+ZINC
51    CONTINUE
      OPEN (UNIT=2,NAME='DK:TRPOF2.DAT',TYPE='NEW')
      WRITE(2,100) ((STRING(K,L),L=1,MP),K=1,MZ)
100   FORMAT(8F10.7)
      STOP
      END
C
C ZEROTH ORDER BESSEL FUNCTION
      FUNCTION BESS(X)
      DOUBLE PRECISION DBESS, DSQRT, DCOS,F,B,Z
      F(Y)=.79788456-.00000077*Y-.00552740*Y**2.-.00009512*Y**3.
     1+.00137237*Y**4.-.00072805*Y**5.+.00014476*Y**6.
      B(Y)=XD-.78539816-.04166397*Y-.00003954*Y**2.
     1-.00054125*Y**4.-.00029333*Y**5.+.00013558*Y**6.
     1+.00262573*Y**3.
      XD=DBLE(X)
1     IF(X.LE.3.)GO TO 2
      Z=3./XD
      DBESS=F(Z)*DCOS(B(Z))/DSQRT(XD)
      BESS=SNGL(DBESS)
      RETURN
2     Z=(XD/3.)*(XD/3.)
      DBESS=1.-2.2499997*Z+1.2656208*Z**2.-.3163866*Z**3.
     1+.0444479*Z**4.-.0039444*Z**5.+.00021*Z**6.
      BESS=SNGL(DBESS)
      RETURN
      END
```

APPENDIX 5

Program TEMPR

The program TEMPR calculates the linear temperature profile in the radial direction and on the sample surface based on Lax's equation with z set to zero:

$$N(R,0,W) = \frac{W}{\sqrt{\Pi}} \int_0^\infty \frac{J_0(\lambda R) e^{-\frac{1}{4}\lambda^2}}{W+\lambda} \, d\lambda \qquad (53)$$

This program differs from the program TEMPRZ (appendix 4) in the following respects: 1) it calculates only radial temperature profile at sample surface, 2) the accuracy of the integration is controlled by automatically increasing the number of divisions in integration until a given accuracy requirement is met (see program listing). This procedure cannot be done in the program TEMPRZ because the running time on the computer would become prohibitively long. Consequently, the results from TEMPR are more accurate.

Following is the program listing for TEMPR.

```
TEMPR
C THIS PROGRAM CALCULATES LINEAR TEMP PROFILE IN RADIAL DIRECTION
C Z IS SET TO ZERO (ON SURFACE OF SAMPLE)
C THE INPUT VARIABLES ARE AS FOLLOWS:
C R2 = MAXIMUM VALUE OF R IN THE TEMPERATURE PROFILE
C M  = NUMBER OF POINTS IN THE TEMP PROFILE
C N  = MINIMUM NUMBER OF DIVISIONS IN THE INTEGRATION
C      N MUST BE EVEN IN SIMPSON'S METHOD
C W  = PRODUCT OF BEAM RADIUS AND ABSORPTION CONSTANT
C VMAX = UPPER LIMIT IN THE INTEGRATION
C ACC = ACCURACY TEST IN THE INTEGRATION : DETERMINES THE APPROPIATE
C       NUMBER OF DIVISIONS FOR INTEGRATION
C OUTPUT IS LINEAR TEMP FILE NAMED TRPOF.DAT
C
C
        DIMENSION STRING(51),T(10)
        LOGICAL*1 ANS
C
C F(Y) IS THE INTEGRAN FROM M.LAX'S THEORY
C
        F(Y)=BESS(Y*R)/(EXP(Y*Y/4.0)*(W+Y))
        TYPE 500
500     FORMAT(//' TYPE IN THE FOLLOWING VALUES:'//
     1 '$MAXIMUM VALUE FOR R IN F4.1 IS=')
        ACCEPT 510,R2
510     FORMAT(F4.1)
        TYPE 800
800     FORMAT('$NUMBER OF POINTS IN R IS (I3):')
        ACCEPT 560,M
560     FORMAT(I3)
        TYPE 600
600     FORMAT('$TYPE NUMBER OF DIVISIONS FOR INTEGRATION:')
        ACCEPT 560,N
        TYPE 700
700     FORMAT('$VALUE OF BEAM WAIST RADIUS*ABS CONST.=')
        ACCEPT 510,W
        TYPE 321
321     FORMAT('$UPPER LIMIT FOR INTEGRATION=?')
        ACCEPT 510,VMAX
        TYPE 79
79      FORMAT('$ACCURACY OF INTEGRATION=')
        ACCEPT 81,ACC
81      FORMAT(F9.7)
        TYPE 34
34      FORMAT('$WANT PRINTED RESULTS?')
        ACCEPT 35,ANS
35      FORMAT(A1)
        IF(ANS .NE. 'Y') GO TO 67
        TYPE 22
22      FORMAT(' ',7X,'R',13X,'TEMPN',9X,'R2')
```

```
C
C SET UP PARAMETERS FOR INTEGRATION
C
67        VMIN=0.0
          FM=M
          PINC=P2/FM
          P=0.0
          J=1
          M=M+1
1         K=1
          FN=N
          NX=N
4         H=VMAX/FN
          TWOH=H+H
          SUM4=0.0
          SUM2=0.0
          X=H
          I=1
2         SUM4=SUM4+F(X)
          SUM2=SUM2+F(X+H)
          IF(I.GE.NX-3) GO TO 3
          I=I+2
          X=X+TWOH
          GO TO 2
C
C TEMPN IS LINEAR TEMP NORMALIZED TO MAXIMUM POSSIBLE VALUE
C AS SUGGESTED BY LAX
C SQUARE ROOT OF PI = 1.7724539
C
3         TEMPN=W*H/3.0*(4.0*SUM4+2.0*SUM2+F(VMIN)+4.0*F(VMAX-H)
     1    +F(VMAX))/1.7724539
C
C DOUBLE NUMBER OF DIVISIONS FOR INTEGRATION
C PROCEDURE REPEATED UNTIL TWO CONSECUTIVE INT. YIELD RESULTS THAT
C AGREE TO WITHIN THE REQUIRED ACCURACY ( ACC )
C
          T(K)=TEMPN
          K=K+1
          FN=FN*2.0
          NX=IFIX(FN+0.5)
          IF(K .LE. 2) GO TO 4
          K2=K-1
          K1=K-2
          IF(ABS(T(K2)-T(K1)) .GT. ACC)GO TO 4
          IF(ANS .NE. 'Y')GO TO 12
          TYPE 11,P,TEMPN,K2
11        FORMAT(' ',2F16.7,I6)
12        STRING(J)=TEMPN
          J=J+1
          P=P+PINC
          IF(P.LE.P2) GO TO 1
```

```
C
C STORE TEMP. PROFILE IN FILE: TO BE USED IN NEXT INTEGRATION
C
        OPEN (UNIT=1,NAME='DK:TPROF.DAT',TYPE='NEW')
        WRITE(1,100) (STRING(J),J=1,M)
100     FORMAT (8F10.7)
        STOP
        END
C
C ZEROTH ORDER BESSEL FUNCTION
C
      FUNCTION BESS(X)
      DOUBLE PRECISION DBESS,DSQRT,DCOS,F,B,Z
      F(Y)=.79788456-.00000077*Y-.00552740*Y**2.-.00009512*Y**3.
     1+.00137237*Y**4.-.00072805*Y**5.+.00014476*Y**6.
      B(Y)=XD-.78539816-.04166397*Y-.00003954*Y**2.
     1-.00054125*Y**4.-.00029333*Y**5.+.00013558*Y**6.
     1+.00262573*Y**3.
      XD=DBLE(X)
    1 IF(X.LE.3.)GO TO 2
      Z=3./XD
      DBESS=F(Z)*DCOS(B(Z))/DSQRT(XD)
      BESS=SNGL(DBESS)
      RETURN
  2   Z=(XD/3.)*(XD/3.)
      DBESS=1.-2.2499997*Z+1.2656208*Z**2.-.3163866*Z**3.
     1+.0444479*Z**4.-.0039444*Z**5.+.00021*Z**6.
      BESS=SNGL(DBESS)
      RETURN
      END
```

APPENDIX 6

Program TTEMPR

This program takes the linear temperatures generated in program TEMPR and converts them into nonlinear temperature profiles: one profile for each nonlinear peak temperature. The temperature conversion curve, which is part of the input to this program, is previously generated in the program TCONV. Following is the program listing for TTEMPR.

```
TTEMPR
C THIS PROGRAM PRODUCES TRUE(NON-LINEAR)  TEMP AS A
C   FUNCTION OF R FOR EACH GIVEN MAXIMUM TEMP.
C OUTPUT IS A TWO-DIMENSIONAL ARRAY TEMP(I,J):
C   I DENOTES TMAX, J DENOTES R
C READ IN ARRAYS LINEAR TMAX,LINEAR TEMP PROFILE,
C   AND TEMP. CONVERSION CURVE
C THE INPUT VARIABLES ARE AS FOLLOWS:
C ARRAY TRPOF(I) IS LINEAR TEMP FROM PROGRAM TEMPR2
C ARRAY TMAXL(I) IS LINEAR MAXINUM TEMP FILE CORRESPONDING
C   TO TRUE TEMPERATURES FROM 300 TO 1650K IN INCREMENTS
C   OF 50 DEGREES
C ARRAY TCONV(I) IS CONVERSION CURVE FROM PROGRAM COND.FOR
C LINEAR INTEPOLATION IS USED IN CONVERSION PROCESS
C
      DIMENSION TEMP(28,51), TRPOF(51), TMAXL(28), TCONV(43)
      OPEN(UNIT=1,NAME='DK:TRPOF.DAT',TYPE='OLD')
      READ (1,100) (TRPOF(I),I=1,51)
100   FORMAT (8F10.7)
      OPEN (UNIT=2,NAME='DK:TFILE.DAT',TYPE='OLD')
      READ (2,200) N,(TMAXL(I),I=1,N)
200   FORMAT (I2/(10F7.2))
      OPEN(UNIT=3,NAME='DK:TCONV.DAT',TYPE='OLD')
      READ (3,300) (TCONV(I),I=1,43)
300   FORMAT (10F7.1)
      DO 1 I=1,N
      DO 2 J=1,51
C
C NORMALIZE TEMP. TO LINEAR MAX. TEMP.
C
      TEMP(I,J)=TMAXL(I)*TRPOF(J)/TRPOF(1)
C
C IA IS TEMP TO THE NEAREST DEGREE
C
      IA=IFIX(TEMP(I,J)+0.5)
C
C CONVERSION TO REAL TEMPERATURES
C
      DO 3 K=1,43
      IF(10*(K-1) .LE. IA)GO TO 3
      RK=10*(K-1)
      TEMP(I,J)=TCONV(K)-(TCONV(K)-TCONV(K-1))*(RK-TEMP(I,J))/10.
      GO TO 2
3     CONTINUE
2     CONTINUE
1     CONTINUE
C
C STORE REAL TEMP PROFILES IN FILE TEMP.DAT FOR
C SUBSEQUENT INTEGRATION
C
      OPEN (UNIT=4,NAME='DK:TEMP.DAT',TYPE='NEW')
      WRITE (4,400) ((TEMP(I,J),J=1,51),I=1,N)
400   FORMAT (10F7.2)
      CLOSE (UNIT=4,DISPOSE='SAVE')
      STOP
      END
```

APPENDIX 7

Program RATIO2

This program uses the temperature profiles computed in the program TTEMPR in calculating Raman ratio as a function of peak temperatures following equation (54):

$$\frac{1}{R_{corr}} = 1 + \frac{1}{2\beta^2}\left[\int_0^\infty nRe^{-R^2\beta^2}\,dR\right]^{-1} \tag{54}$$

The program listing for RATIO2 follows:

```
RATIO2
C THIS PROGRAM CALCULATES RAMAN RATIO AS A FUNCTION
C    OF MAXIMUM TEMP AT BEAM CENTER
C THE INPUT VARIABLES ARE AS FOLLOWS:
C ARRAY TEMP(I,J) IS TRUE TEMPERATURE PROFILES CALCULATED
C    IN THE PROGRAM TTEMPR
C N = NUMBER OF POINTS IN THE RAMAN RATIO - TEMP CURVE
C RINC = INCREMENTS IN R IN THE INTEGRATION. IT IS
C    DICTATED BY NUMBER OF POINTS IN THE TEMP PROFILE
C COR = RATIO OF HEAT BEAM RADIUS TO PROBE BEAM RADIUS
C
      DIMENSION TEMP(28,51)
      TYPE 100
100   FORMAT (' THIS PROGRAM CALCULATES A-STOKES TO STOKES RATIO'/
     1' INPUT IS TEMP.DAT FILE. R VALUES 0 TO 3 IN RINC INCREMENTS')
      TYPE 200
200   FORMAT (' TYPE IN THE NUMBER OF POINTS FOR TEMP-RATIO CURVE:')
      ACCEPT 300,N
300   FORMAT (I2)
      TYPE 29
29    FORMAT('$INCREMENTS IN R = ')
      ACCEPT 32,RINC
32    FORMAT(F5.3)
      OPEN (UNIT=1,NAME='DK:TEMP.DAT',TYPE='OLD')
      READ (1,400) ((TEMP(I,J),J=1,51),I=1,N)
400   FORMAT (10F7.2)
      TYPE 68
68    FORMAT('$CORRECTION FACTOR=HEAT BEAM/PROBE BEAM= ')
      ACCEPT 39,COR
39    FORMAT(F9.7)
      CORI=1./COR
      DO 1 I=1,N
      R=0.0
      DO 2 J=1,51
C
C POP IS POPULATION FACTOR
C 747.27 IS EXPONENTIAL FACTOR (EXCEPT TEMP) FOR 519
C WAVENUMBER PHONON
C
      POP=1./(EXP(747.27/TEMP(I,J))-1.)
      TEMP(I,J)=R*POP/EXP(COR*COR*R*R)
2     R=R+RINC
      SUM2=0.0
      SUM4=0.0
      DO 3 K=2,48,2
      SUM4=SUM4+TEMP(I,K)
3     SUM2=SUM2+TEMP(I,K+1)
      RATIO=1.0+CORI*CORI*3.0/(2.0*RINC*(TEMP(I,1)+4.0*SUM4+2.0*SUM2
     1+4.0*TEMP(I,50)+TEMP(I,51)))
      RATIO=1.0/RATIO
1     TYPE 500,RATIO
500   FORMAT(F16.7)
      STOP
      END
```

APPENDIX 8

Program RTCONV

Using the Raman ratio vs. Peak temperature curve generated in program RATIO2, this program converts the experimentally obtained Raman ratios into peak temperatures. The listing of program RTCONV follows:

```
RTCONV
C THIS PROGRAM CONVERTS RAMAN A-S RATIO INTO MAX TEMP
C INPUT VARIABLES ARE AS FOLLOWS:
C ARRAY RATIO(I) IS DATA FILE OF THE EXPERIMENTALLY
C   OBTAINED RAMAN RATIOS
C CONV(I) IS ARRAY OF POINTS IN THE RATIO-TEMP
C CONVERSION ; THEY ARE RESULTS FROM PROGRAM RATIO2
C LINEAR INTERPOLATION IS USED IN CONVERSION PROCESS
C RESULTS ARE ROUNDED TO NEAREST DEGREE
C
      DIMENSION RATIO(40), CONV(30)
      LOGICAL*1 FILER(15),FILEC(15)
      CALL GTLIN (FILER,'TYPE FILENAME OF RAMAN RATIO,DK:FILNM.TYP')
      CALL GTLIN (FILEC,'TYPE NAME OF CONVERSION FILE,DK:FILNM.TYP')
      OPEN (UNIT=1,NAME=FILER,TYPE='OLD')
      READ(1,100) N,(RATIO(I),I=1,N)
      OPEN (UNIT=2,NAME=FILEC,TYPE='OLD')
      READ(2,200) W,(CONV(I),I=1,28)
100   FORMAT(I2/(8F10.7))
200   FORMAT(F4.1/(8F10.7))
      TYPE 300,W
300   FORMAT(' ',' BEAM RADIUS W= ',F4.1)
      DO 1 I=1,N
      DO 2 J=1,28
      IF(CONV(J) .LE. RATIO(I))GO TO 2
      FJ=J
      T=(FJ-1.)*50.+300.
      TEMP=T-50.*(CONV(J)-RATIO(I))/(CONV(J)-CONV(J-1))
      ITEMP=IFIX(TEMP+0.5)
      TYPE 400,RATIO(I),ITEMP
400   FORMAT(' ',F10.7,I10)
      GO TO 1
2     CONTINUE
1     CONTINUE
      STOP
      END
```

APPENDIX 9

Program TPOWD

This program computes the theoretical peak temperature vs. power density (P/a) curve following equation of Lax:

$$\Theta(0,0,W) = \left(\frac{P}{a}\right) \frac{1}{2\sqrt{\pi}K_o} N(0,0,W) \tag{41}$$

The value of N(0,0,W) was computed previously as a part of the results in program TEMPR. Following is the program listing for the program TPOWD.

```
TPOWD
C THIS PROGRAM CALCULATES MAX TEMP AS A FUNCTION
C   OF POWER DENSITY
C INPUT VARIABLES ARE AS FOLLOWS:
C TMAXL(I) IS ARRAY OF LINEAR MAX TEMP CORRESPONDING
C   TO REAL TEMP OF 300 TO 1650K IN 50 DEGREE INCREMENTS
C N = NUMBER OF POINTS IN THE TMAXL FILE
C W = PRODUCT OF BEAM RADIUS AND ABSORPTION CONSTANT
C FAC = LINEAR MAX TEMP FOR A GIVEN W
C FAC IS FOUND IN RESULTS OF PROGRAM TEMPR2
C
      DIMENSION TMAXL(30)
      OPEN(UNIT=1,NAME='TFILE2.DAT',TYPE='OLD')
      READ(1,100) N,(TMAXL(I),I=1,N)
100   FORMAT(I2/(10F7.2))
      CLOSE(UNIT=1,DISPOSE='SAVE')
      CALL PRINT (' TYPE IN VALUE OF W IN F4.1 ')
      ACCEPT 200
200   FORMAT(F4.1)
      CALL PRINT (' TYPE IN VALUE OF N(0,0,W) IN F9.7 ')
      ACCEPT 300,FAC
300   FORMAT(F9.7)
      SPP=SQRT(3.1415927)
      DO 1 I=1,N
C
C VALUE OF THERMAL CONDUCTIVITY AT ROOM TEMP = 1.48
C
      PD=TMAXL(I)*2.0*SPP*1.48/FAC
1     TYPE 440,TMAXL(I),PD
440   FORMAT(' ',2F16.7)
      STOP
      END
```

REFERENCES

1. Science 201, 333 (1978).

2. Physics Today, July 1978, p. 17.

3. G. A. Kachurin, N. B. Pridachin, and L. S. Smirnov, Sov. Phys. - Semicond. 9, 946 (1975).

4. E. I. Shtyrkov, I. B. Khaibullin, M. M. Zaripov, M. F. Galyatudinov, and R. M. Bayazitov, Sov. Phys. - Semicond. 9, 1309 (1975).

5. J. C. C. Fan, R. L. Chapman, J. P. Donnelly, G. W. Turner, and C. O. Bozler, Appl. Phys. Lett. 34 (11), 780 (1979) and references therein.

6. A. G. Klimenko, E. A. Klimenko, and V. I. Donin, Sov. J. Quantum Electron. 5, 1289 (1976).

7. G. A. Kachurin, E. V. Nidaev, A. V. Khodyaçhikh, and L. A. Kovaleva, Sov. Phys. - Semicond. 10, 1128 (1976).

8. R. T. Young, C. W. White, G. J. Clark, J. Narayan, W. H. Christie, M. Murakami, P. W. King, and S. D. Kramer, Appl. Phys. Lett. 32 (3), 139 (1978).

9. G. K. Celler, J. M. Poate, and L. C. Kimerling, Appl. Phys. Lett. 32 (8), 464 (1978).

10. A. Gat, J. F. Gibbons, T. J. Magee, J. Peng, P. Williams, V. Deline, and C. A. Evans, Jr., Appl. Phys. Lett. 33 (5), 389 (1978).

11. J. S. Williams, W. L. Brown, J. J. Leamy, J. M. Poate, J. W. Rodgers, D. Rousseau, G. A. Rozgonyi, J. A. Shelnutt, and T. T. Sheng, Appl. Phys. Lett. 33 (6), 542 (1978).

12. Y. S. Liu and K. L. Wang, Appl. Phys. Lett. 34 (6), 363 (1979) and references therein.

13. D. H. Auston, J. A. Golovchenko, A. L. Simons, C. M. Surko, and T. N. C. Venkatesan, Appl. Phys. Lett. 34 (11), 777 (1979).

14. Bull. Am. Phys. Soc. 24 (3), 314 (1979).
15. M. Lax, J. Appl. Phys. 48, 3919 (1977).
16. M. Lax, Appl. Phys. Lett. 33 (8), 786 (1978).
17. C. M. Surko, A. L. Simons, O. H. Auston, J. A. Golovchenko, R. E. Slusher, and T. N. C. Venkatesan, Appl. Phys. Lett. 34 (10), 635 (1979) and references therein.
18. R. Loudon, Proc. Roy. Soc. A275, 218 (1963).
19. R. Loudon, Adv. in Phys. 13, 423 (1964).
20. See for example E. Merzbacher, Quantum Mechanics (2nd. ed., John Wiley and Sons, Inc., New York, 1970) P. 465.
21. J. B. Renucci, R. N. Tyte, and M. Cardona, Phys. Rev. B 11, 3885 (1975).
22. P. Temple and C. Hathaway, Phys. Rev. B 7, 3685 (1973) and references therein.
23. T. R. Hart, R. L. Aggarwal, and B. Lax, Phys. Rev. B 1, 638 (1970).
24. E. Anastassakis, H. C. Hwang, and C. H. Perry, Phys. Rev. B 4, 2493 (1971).
25. C. Y. Ho, R. W. Powell, and P. E. Liley, J. Phys. Chem. Ref. Data, Vol. 3, Suppl. 1, 588 (1974).
26. See for example H. S. Carslaw and J. C. Jaeger, Conduction of Heat in Solids (Oxford U. P., London, 1947) P. 6.
27. See for example P. M. Morse and H. Feshbach, Methods of Theoretical Physics (McGraw Hill, New York, 1953) P. 944.
28. W. C. Dash and R. Newman, Phys. Rev. 99, 1151 (1955).
29. J. F. Ready, Effects of High Power Laser Radiation (Academic Press, Inc., New York, 1971) P. 20.
30. B. A. Weinstein and G. J. Piermarini, Phys. Rev. B 12 (4), 1172 (1975).
31. E. Anastassakis, A. Pinczuk, and E. Burstein, Solid State Comm. 8, 133 (1970).

32. M. Abramowitz and I. A. Stegun, ed., Handbook of Mathematical Functions (Dover Publications, Inc., New York, 1972).

RAMAN MEASUREMENTS OF TEMPERATURE DURING CONTINUOUS WAVE LASER-INDUCED HEATING OF SILICON

by

HO WAI LO

B.S., North Texas State University, 1976

AN ABSTRACT OF A MASTER'S THESIS

submitted in partial fulfillment of the

requirements for the degree

MASTER OF SCIENCE

Department of Physics

KANSAS STATE UNIVERSITY

Manhattan, Kansas

1979

The temperature rise in a pure silicon wafer during continuous heating by an argon ion laser has been measured, in situ, by analyzing the anti-Stokes to Stokes intensity ratio of the first order phonon Raman line. Laser beam spots with Gaussian intensity profiles were used. Application of a wide range of laser power levels produced peak temperatures ranging from room termperature to the melting point. The effect of non-uniform temperatures across the heated area was deconvoluted by using theoretically calculated temperature gradients in the data reduction process. The resulting peak temperatures agree well with theoretical predictions based on Lax's solutions to the nonlinear heat diffusion equation when adjustments are made to the temperature-sensitive absorption constant. The Raman data also show evidence of strain effects on the sample at elevated temperatures.